JGR Earth Surface

METHOD

10.1029/2025JF008475

Subglacial Conditions From Converted-Wave Seismic Reflection Amplitudes: Synthetic Experiments and Case Study Reveal a Frozen Bed at an Antarctic Ice Rise

Ronan S. Agnew[1,2], **Adam D. Booth**[1], **Alex M. Brisbourne**[2], **Roger A. Clark**[1], **Philip W. Livermore**[1], **and Andrew M. Smith**[2]

[1]School of Earth and Environment, University of Leeds, Leeds, UK, [2]British Antarctic Survey, Cambridge, UK

Key Points:

- The value of jointly inverting seismic PP and PS-wave reflectivity for glaciological studies has been investigated using synthetic data
- Joint inversion improves precision and accuracy in constraining subglacial properties - degree of improvement varies with subglacial regime
- Joint inversion of PP and PS AVA data from Korff Ice Rise, West Antarctica, reveals basal properties consistent with a frozen bed

Correspondence to:

R. S. Agnew,
rognew91@bas.ac.uk

Citation:

Agnew, R. S., Booth, A. D., Brisbourne, A. M., Clark, R. A., Livermore, P. W., & Smith, A. M. (2025). Subglacial conditions from converted-wave seismic reflection amplitudes: Synthetic experiments and case study reveal a frozen bed at an Antarctic ice rise. *Journal of Geophysical Research: Earth Surface*, *130*, e2025JF008475. https://doi.org/10.1029/2025JF008475

Received 3 APR 2025
Accepted 25 NOV 2025

Abstract Estimating the seismic reflectivity of the glacial ice-bed interface is a powerful means to quantify subglacial properties, which is important for parameterizing sliding laws in ice sheet models and understanding ice sheet history. Amplitude-versus-angle (AVA) analysis measures reflectivity with incidence angle and is sensitive to the compressional and shear properties of the interface. Conventional AVA inversions use only reflected compressional (PP) components and are nonunique; joint inversion using compressional-to-shear mode conversions (PS) may mitigate this and boost the information return from a seismic survey campaign. We present an inversion scheme which inverts PP and PS-wave AVA data for subglacial properties. Using synthetic AVA data for diverse subglacial regimes, we evaluate its performance when inverting PP data only, and jointly inverting PP and PS data, for narrow- and wide-angle geometries. For the same angular range, joint inversion improves upon single inversion in both precision and accuracy; furthermore, narrow-angle joint inversion performs comparably or favorably when compared to wide-angle single inversion. Joint inversion improves constraint of bed properties most when subglacial materials have high Poisson's ratios. We apply the inversion scheme to data from Korff Ice Rise, West Antarctica, and find basal properties consistent with a frozen bed; single and joint inversion results are comparable. Best estimates of $Z = (5.79 \pm 0.26) \times 10^6$ kg m^{-2}s^{-1} and $\sigma = 0.298 \pm 0.010$ are taken from joint inversion of wide-angle data. We consider joint PP/PS inversion a means to utilize fully the seismic wavefield when multicomponent acquisition complements other survey aims, but care should be taken when substituting wide-angle with multicomponent data.

Plain Language Summary Understanding how an ice sheet slips at its base is an important part of ice sheet models; this requires knowledge of the geological materials underlying the ice. Controlled-source seismic surveys which estimate the amplitude of the seismic waves reflected from the ice base are a common means of inferring the properties of these materials. Typically, these surveys are sensitive to reflected compressional (PP) waves only; this excludes important information contained in the waves converted to shear waves (PS) when reflected at the ice base. This study investigates how inferences of glacier bed properties may be improved by joint analysis of PP and PS waves. Using synthetic data, we demonstrate that joint analysis improves upon the conventional method in both precision and accuracy. Analysis of PS waves may allow accurate ice base properties to be retrieved using smaller survey geometries than those intended for PP analysis only. Our method provides the greatest improvement when soft sediment or water is beneath the ice. We apply the method to data from Korff Ice Rise, West Antarctica, inferring that the ice base is frozen.

1. Introduction

Glacier and ice sheet flow velocities depend on a complex interaction between ice rheology, subglacial topography, subglacial hydrology and subglacial material properties. Beneath the ice streams which drain West Antarctica, the presence and distribution of deforming subglacial till and "sticky spots" of stiffer tills and bedrock are important controls on ice stream flow velocities and ice sheet stability (e.g., Anandakrishnan & Alley, 1997; Catania et al., 2006; Parizek et al., 2013; Peters et al., 2006; Smith, 1997b). Ice sheet models are typically initialized with basal conditions inverted from ice surface velocities; however, inverted bed conditions can be contradicted by field observations (e.g., Bougamont et al., 2014; Harper et al., 2017). Model projections are highly sensitive to the distribution and type of bed material (Parizek et al., 2013). This highlights the need of continued geophysical observations of the subglacial environment to help inform model processes.

Controlled-source seismic studies are particularly sensitive to the material properties of the subglacial environment. Where a reflection is observed at the interface between a subglacial till and an underlying layer, measurement of the interval velocity can yield inferences of porosity and effective pressure (e.g., Blankenship et al., 1987). Where this is not possible, subglacial properties may be inferred from the amplitude of the seismic return from the ice-bed interface. Commonly, these experiments aim to distinguish materials by measurement of the acoustic impedance, Z, at the bed, via the reflection coefficient at normal incidence, R_0. This is a well-established technique for identifying subglacial materials, and has frequently been applied beneath Antarctic ice streams (e.g., Brisbourne et al., 2017; Clyne et al., 2020; Muto et al., 2019; Smith, 1997a). Normal-incidence reflectivity techniques enable measurement of basal properties at many locations along a seismic line, providing a means of assessing the distribution of subglacial materials (Smith, 1997b). However, they are sensitive only to acoustic impedance contrasts, as at normal incidence no energy is converted to shear (S) waves. Despite recent progress in this area (Hank et al., 2025), incorporating acoustic impedance directly into ice-sheet models remains difficult (Kyrke-Smith et al., 2017), and in many cases it is beneficial to constrain subglacial properties further by measurement of Poisson's ratio, σ, which is related to porosity. Amplitude-versus-offset (AVO), or amplitude-versus-angle (AVA), techniques deliver more comprehensive measurements of the bed's material properties due to their sensitivity to both Z and σ.

AVA techniques quantify the reflection coefficient R as a function of incidence angle θ. In glaciology, they have been used to identify basal materials underneath ice streams and outlet glaciers in Antarctica (Anandakrishnan, 2003; Horgan et al., 2021; Peters et al., 2007) and Greenland (Hofstede et al., 2018; Kulessa et al., 2017), as well as mountain glaciers (Zechmann et al., 2018). They can be used to identify interference effects arising from thinly layered substrates (Booth et al., 2012), and have also been used to characterize transient changes in subglacial conditions (Kulessa et al., 2017; Nolan & Echelmeyer, 1999). The sensitivity of AVA methods to the presence of subglacial water makes them excellent methods for investigating possible subglacial lake locations (Peters et al., 2008); recent work has shown that inference of subglacial lakes from radio echo-sounding may be refuted by seismic measurements owing to the latter technique's greater sensitivity to basal properties, highlighting the continued need for surveys which use multiple geophysical methods (Hofstede et al., 2023; Killingbeck et al., 2024).

AVA inversions which use only the compressional (P) wave component of the wavefield and ignore the shear (S) component are highly nonunique (Castagna & Backus, 1993). As multicomponent recording and joint active- and passive-source experiments using technologies such as 3-component seismic nodes proliferate (e.g., Agnew et al., 2025; Labedz et al., 2022; Veitch et al., 2021), data sets which include high-quality records of S-waves and P to S-wave mode conversions (converted, or PS-waves) will become more common. Converted wave AVA has been applied to characterization of hydrocarbon reservoirs (e.g., Kurt, 2007; Lu et al., 2015; Ramos & Castagna, 2001), and joint inversion approaches have been shown to be more accurate than sole analysis of P-wave reflection amplitudes (Ursenbach, 2005). The extent to which the inclusion of converted waves may mitigate nonuniqueness in glaciological AVA inversions is currently under-explored.

We address these knowledge gaps by presenting an inversion scheme for jointly inverting amplitudes of compressional and converted waves reflected from the glacier bed. Using synthetic data, we investigate the extent to which this improves elastic property estimation over conventional (P-wave only) methods. We then implement the method on data from Korff Ice Rise (KIR), West Antarctica, discussing the glaciological implications of the observed AVA response and inverted basal properties. In so doing, we identify the cases in which seismic data acquired for AVA analysis benefit most from investing field effort in extending to long source-receiver offsets, or instead using multicomponent geophones.

2. The AVA Method for Converted Phases

2.1. The AVA Method

When a seismic wave is incident on an interface between two media, the energy is partitioned into reflected and transmitted waves. This partitioning was described for body waves in terms of potentials by Knott (1899), and subsequently in terms of displacement amplitudes by Zoeppritz (1919). When a compressional (P) wave is obliquely incident on an interface, some of its energy is converted into transmitted and reflected shear (S) waves (Figure 1a). The proportion of energy partitioned into each of the reflected and transmitted P and S phases is dependent on the incidence angle θ and the elastic properties (density, P-wave velocity, S-wave velocity) of the

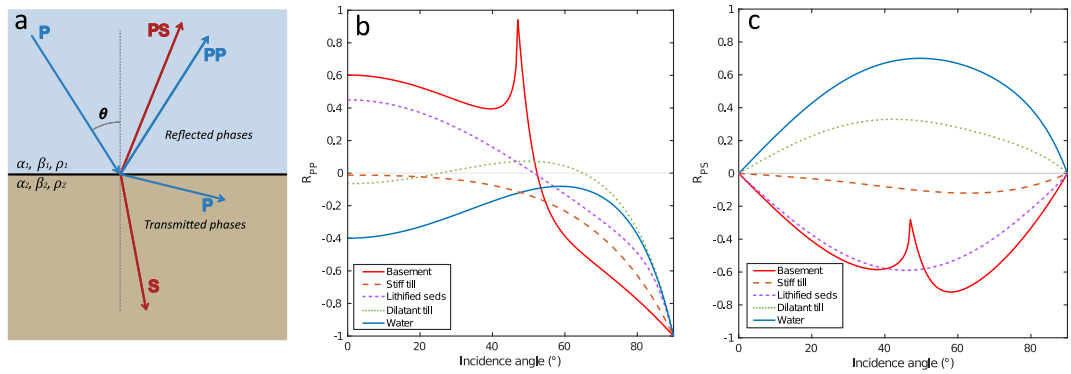

Figure 1. (a) Partition of energy into reflected and transmitted compressional and shear waves at an interface between two media of contrasting elastic properties. (b) PP and (c) PS and responses for the glacier bed materials detailed in Table 1.

two media. The fundamental principle of amplitude-versus-angle (AVA) techniques is to deduce the elastic properties from measurements of the offset- or angle- dependence of $R(\theta)$.

The amplitude A of a wavelet arriving at a receiver a distance x from the source, having reflected from an interface, is:

$$A(x,f) = A_0(f)R(x)\gamma(x)e^{-a(f)r(x)}. \quad (1)$$

here, A_0 is the source amplitude, f is frequency, and R describes the effect of reflectivity along the ray path, which has length $r(x)$. γ describes geometrical spreading factors and a is the absorption coefficient, $a(f) = \pi f/Qv$. Q is the seismic quality factor (assumed frequency-independent) and v the velocity of the wavelet. For the purposes of making amplitude corrections when Q and v vary over the ray path, it is useful to make the substitution $t^* = t/Q$, where t is propagation time. t^* is called the attenuated time (Carpenter et al., 1966) and is cumulative along the ray path. $R(\theta)$ can be estimated using:

$$R(\theta) = \frac{A(\theta)}{A_0}\frac{1}{\gamma(\theta)}e^{\pi f t^*(\theta)}. \quad (2)$$

The Knott-Zoeppritz (KZ) equations describe $R(\theta)$ in terms of the elastic parameters either side of the interface: P-wave velocities α_1 and α_2, S-wave velocities β_1 and β_2, and densities ρ_1 and ρ_2 (subscript "1" denotes the incident side). For each side of the interface, these properties can be combined into the two quantities acoustic impedance Z and Poisson's ratio σ. The quantity Z is related to the density (ρ) and P-wave velocity (α) of a material by

$$Z = \rho\alpha. \quad (3)$$

Poisson's ratio is related to the P and S-wave velocities of a material by

$$\sigma = \frac{\alpha^2 - 2\beta^2}{2(\alpha^2 - \beta^2)}. \quad (4)$$

The term "converted wave" in general applies to any mode conversion, whether P to S or S to P upon transmission or reflection. From here on it refers only to the reflected PS-wave, that is, a downgoing P-wave converted to an upgoing S-wave at a reflecting interface. We refer to a downgoing P-wave reflected as a P-wave as "PP."

To estimate the reflection coefficient of a P-to-S converted wave, we deal with the P-wave and S-wave portions of the propagation path separately:

$$R_{PS}(\theta) = \frac{A_{PS}(\theta)}{A_0}\frac{1}{\gamma_P(\theta)\gamma_S(\theta)}e^{\pi f t_P^*(\theta)}e^{\pi f t_S^*(\theta)}, \quad (5)$$

Table 1
Example Properties of Bed Materials Simulated—P-Wave Velocity α, S-Wave Velocity β, Density ρ, Acoustic Impedance Z and Poisson's Ratio σ

Material	α (m s^{-1})	β (m s^{-1})	ρ (kg m^{-3})	Z (10^6 kg m^{-2} s^{-1})	σ
Ice[a,b]	3,810	1,860	920	3.5	0.34
Water[b]	1,500	0	997	1.5	0.5
Basement[b]	5,200	2,800	2,700	14	0.3
Lithified sediment[b]	3,750	2,450	2,450	9.19	0.128
Stiff till[a]	1,800 ± 150	1,000 ± 100	1,900 ± 150	3.42 ± 0.4	0.28 ± 0.08
Dilatant till[a, c]	1,700 ± 150	200 ± 50	1,800 ± 150	3.06 ± 0.4	0.49 ± 0.004

Note. AVA responses of these materials are displayed in Figure 1. [a]Properties taken from Peters et al. (2007). [b]Properties taken from Christensen (1989). [c]Properties taken from Peters et al. (2008).

where γ_P is the geometric spreading factor applied to the P-wave portion of the ray path, γ_S is the geometric spreading factor applied to the S-wave portion, t_P^* is the wavelet's attenuated time as a downgoing P-wave, and t_S^* is its attenuated time as an upgoing S-wave.

2.2. Glaciological PP and PS AVA Responses

Figures 1b and 1c show the angle-dependent reflectivity $R(\theta)$ for some previously reported glacial substrates. Note that this figure shows only $R(\theta)$ and not surface-recorded AVA responses. AVA responses are computed from the properties in Table 1, after Peters et al. (2008). Together, these materials represent as wide a range of subglacial materials a glaciological AVA survey is likely to encounter. Subglacial water may be identified, and water column depth measured, under ice shelves (e.g., Horgan et al., 2021), at subglacial lakes (e.g., Brisbourne et al., 2023), or in other locations where the subglacial hydrological system allows water pooling. "Basement" refers to crystalline bedrock, and lithified sediment can be interpreted as sedimentary rock. "Stiff till" is used to mean a wet, low porosity till which is not deforming (Peters et al., 2007). During streaming, saturated subglacial till dilates, causing an increase in till porosity (Boulton & Dent, 1974; Boulton et al., 1974; Boulton & Paul, 1976); this is referred to as dilatant till. The peaks in the AVA responses for ice/basement at $\sim 45°$ represent the critical angle θ_{crit} of the incident wave (Figures 1a and 1b). The Knott-Zoeppritz equations do not account for critically refracted waves, so amplitudes at angles approaching $\theta \geq \theta_{\text{crit}}$ should not be used (Červený, 1966).

Glaciological AVA studies invert for the basal properties which give the minimum misfit to a PP AVA response. However, these inversions are highly nonunique, especially when the available angular range of data is limited; commonly, $\theta < 30°$ (e.g., Booth et al., 2012; Booth et al., 2016; Horgan et al., 2021). Jointly inverting PP and PS AVA data may help to reduce this nonuniqueness because the PP and PS AVA responses contain different information about the substrate. Furthermore, because the upgoing S-wave travels at a slower velocity than the downgoing P-wave, the PS ray path is asymmetric, and a converted wave is incident at a larger angle than the PP-wave detected at the same receiver. Analyzing PS-waves is a means of extending the angular coverage of incident waves at the glacier bed for a fixed seismic acquisition layout, and offers an independent subset of seismic data with which to constrain material properties.

3. Synthetic Experiments

3.1. Inversion Scheme and Experimental Design

We use a Bayesian Markov chain Monte-Carlo (MCMC) inversion scheme similar to others reported for other applications to glaciological problems (e.g., Booth et al., 2012; Killingbeck et al., 2018) and hydrocarbon reservoir characterization (e.g., He et al., 2022; Pan et al., 2017), implementing the Metropolis-Hastings (MH) algorithm (Hastings, 1970; Metropolis et al., 1953). Bayes' theorem expresses that the posterior probability $\mathrm{P}(\mathbf{m}|\boldsymbol{d})$ of a candidate model $\mathbf{m}$ given observed data $\boldsymbol{d}$ is proportional to the product of the prior $\mathrm{P}(\mathbf{m})$ and the likelihood $\mathrm{P}(\boldsymbol{d}|\mathbf{m})$:

$$\mathrm{P}(\mathbf{m}|\boldsymbol{d}) \propto \mathrm{P}(\mathbf{m})\mathrm{P}(\boldsymbol{d}|\mathbf{m}). \quad (6)$$

In AVA analysis, $\boldsymbol{d} = R(\theta)$ contains AVA data and $\mathbf{m} = [\rho_1, \rho_2, \alpha_1, \alpha_2, \beta_1, \beta_2]$ contains the densities (ρ_1, ρ_2), P-wave velocities (α_1, α_2) and S-wave velocities (β_1, β_2) on either side of a reflective interface. P($\mathbf{m}$) describes the a priori knowledge of the system. For our purposes, "1" subscripts are glacial and "2" subscripts are subglacial.

The MCMC algorithm constructs a long chain of models, whose statistics converge to those of the sought posterior distribution. To form a chain, a starting model $\mathbf{m}$ is defined. Its seismic response $\boldsymbol{g}(\mathbf{m})$ is modeled using the KZ equations, and the likelihood of $\mathbf{m}$ is calculated based on the misfit of $\boldsymbol{g}(\mathbf{m})$ to the observed data $R(\theta)$. The posterior probability P($\mathbf{m}|\boldsymbol{d}$) is then evaluated. A Gaussian perturbation is applied to $\mathbf{m}$ to produce a new candidate model, $\mathbf{m}'$, and P($\mathbf{m}'|\boldsymbol{d}$) is computed. In our implementation, the magnitude of the perturbation is $\sim$20 ms^{-1} in velocity and $\sim$20 kg m^{-3} in density. The acceptance probability P(accept) determines whether a candidate model is accepted or rejected:

$$\mathrm{P(accept)} = \frac{\mathrm{P}(\mathbf{m}'|\boldsymbol{d})}{\mathrm{P}(\mathbf{m}|\boldsymbol{d})} \tag{7}$$

If P(accept) > 1, $\mathbf{m}'$ is accepted and used as the starting point for the next perturbation. Otherwise, $\mathbf{m}'$ is accepted with the probability P(accept). If$\mathbf{m}'$ is not accepted then $\mathbf{m}$ is replicated and used again as the next starting model in the chain. For a large ensemble, the distribution of explored models converges to the posterior distribution. The median and quartiles of Z and σ are then computed from their marginal distributions (i.e., considered independently). The breadth of these interquartile ranges is a measure of the nonuniqueness of the inversion.

We set flat priors (i.e., a uniform distribution) between reasonable bounds for the subglacial material, outside which the posterior probability is zero: the density is assumed uniformly distributed in the range $920 \leq \rho_2 \leq 4000$ kg m^3, the P-wave velocity is assumed uniformly distributed between 0 and 8000 m s^{-1} and the S-wave velocity is assumed uniformly distributed between 0 and 5000 m s^{-1}. Poisson's ratio must lie within $0 \leq \sigma_2 \leq 0.5$ for plausible glaciological materials. Basal ice properties are constrained to previous measurements (Peters et al., 2008) with assumed Gaussian distributions: $\rho_1 = 920 \pm 20$ Kg m^{-3}; $\alpha_1 = 3810 \pm 20$ m s^{-1}; $\beta_1 = 1860 \pm 20$ m s^{-1}. The inversion outputs running medians of bed acoustic impedance and Poisson's ratio to check for convergence. The inversion scheme uses a burn-in period of 10,000 iterations from which the models are not included in the posterior distribution. For noiseless synthetic data, the running medians do not change significantly after 1,000,000 iterations, so we use chains of 2,000,000 iterations for our synthetic tests.

We run the inversion in two configurations, for inverting (a) PP AVA data only, and (b) PP and PS AVA data jointly. The likelihood P($\boldsymbol{d}|\mathbf{m}$) depends on the error-weighted residuals of the AVA response of the model to the data:

$$\mathrm{P}(\boldsymbol{d}|\mathbf{m}) = \exp\left[-\frac{1}{2}\sum_i \left(\frac{R^i_{PP} - g^i_{PP}(\mathbf{m})}{\epsilon^i_{PP}}\right)^2 - \frac{1}{2}\sum_i \left(\frac{R^i_{PS} - g^i_{PS}(\mathbf{m})}{\epsilon^i_{PS}}\right)^2\right]. \tag{8}$$

R^i is the ith data point in a measured PP AVA response, $g^i(\mathbf{m})$ is the ith data point in a synthetic AVA response for a given model $\mathbf{m}$, and ϵ^i is the uncertainty in R^i. Subscripts PP and PS denote modes of propagation. For single PP inversion, the second term is ignored. This likelihood assumes that measurements of PP and PS are independent, given a model. We evaluate the performance of the inversions using two metrics: the distance of the medians from the known solution, and the width of the posterior distribution of Z and σ, quantified by the interquartile range. We compare the performance of the inversion when given (a) PP AVA responses only, and (b) PP and PS AVA responses.

We use synthetic AVA data generated from the exact KZ equations for ice overlying each of water, basement rock, stiff till, dilatant till and lithified sediment, after Peters et al. (2007, 2008). AVA inversions suffer from nonuniqueness resulting not only from noisy data, but also partly from the tradeoff between ρ and α as they combine in the acoustic impedance. To investigate the extent to which joint inversion mitigates this nonuniqueness alone, rather than uncertainty arising from noise, we use synthetic AVA data with no noise. However, a systematic standard deviation of $\epsilon_{PP} = \epsilon_{PS} = 0.2$ is imposed on $R(\theta)$ for the purposes of computing a likelihood. This corresponds with typical uncertainties in field AVA data (e.g., Peters et al., 2008). This uncertainty may be an underestimate for large-magnitude reflectivities but an overestimate for small-magnitude

reflectivities, since ϵ typically scales with R. To investigate the extent to which joint inversion improves results for varying survey geometries, we test the inversions for two survey geometries: (a) a "narrow-angle" survey, from $0 \leq 30°$, and (b) a "wide-angle" survey from $0 \leq 60°$. An incident P-wave at an ice/basement interface critically refracts at $\theta = 46°$, so we truncate this AVA response to $0 \leq \theta < 46°$.

3.2. Example of Inversion Output

To demonstrate the ability of the inversion scheme to retrieve known bed properties, we give an example of the inversion output for a bed of lithified sediments (see Table 1), given noiseless synthetic PP and PS AVA responses. Figure 2a shows the input AVA responses, along with the PP and PS AVA responses of the median model found. The PP and PS AVA responses contain data at intervals of 0.5° from 0° to 60°. Figure 2b shows the marginal distributions of density, P-wave velocity and S-wave velocity for the bed, with model values and distribution medians marked by black dotted lines and yellow dashed lines, respectively. When viewed as a combination of ρ, α and β separately, the distributions of estimated bed properties are complicated, being multimodal for α and β. It is difficult for the inversion to resolve these variables; the median inverted properties of $\rho_2 = 2778$ kg m^{-3}, $\alpha_2 = 3232$ m s^{-1} and $\beta_2 = 2123$ m s^{-1} have a mean deviation of $\sim$13% from the true model values (yellow dotted lines compared to dashed black lines in Figure 2b). The AVA responses of the median model are shown as dotted curves in Figure 2a. This illustrates the difficulty of retrieving α, β and ρ: the predicted AVA responses from the median properties are indistinguishable from the true ones, despite the deviation in median α, β and ρ from their true values.

In contrast, bed properties expressed as Z and σ are better resolved (Figure 2c): the median and quartiles from these distributions imply $Z = (9.07 \pm 0.30)$ kg m^{-2}s^{-1} and $\sigma = 0.13 \pm 0.08$, which have a mean deviation of 2% from the true values (Table 1). This demonstrates that the inversion is effective at recovering known basal acoustic impedances and Poisson's ratios; consequently, when comparing the performances of single and joint inversion under different survey parameters, we quote the medians and quartiles of the marginal distributions of Z and σ and are careful not to overinterpret inversions for ρ, α and β.

3.3. Comparison of PP and Joint Inversion

Figure 3 summarizes the results of the single and joint inversions for the five basal regimes (see Table A1 in Appendix A for details). The acoustic impedances and Poisson's ratios of the reference materials (Table 1) are plotted alongside the inversion results to enable identification of the basal regime. The inversion scheme is effective in retrieving known basal properties. However, interpretation of results obtained using the narrow single inversion (Figure 3a) may still be ambiguous, especially for beds of till, as the posterior distributions for Poisson's ratio overlap for stiff and dilatant till. Substrate identification becomes less ambiguous when jointly inverting or adding wider angle data: comparing Figures 3a–3d, uncertainties reduce when going from narrow single inversion to wide or joint inversions and in general medians approach the known solutions. Furthermore, panels b and c show that narrow joint inversion of $\theta \leq 30°$ data delivers comparable results of to those obtained by wide single inversion of $\theta \leq 60°$ data. It is clear that joint inversion has the potential to reduce ambiguity in glacial substrate identification, potentially with no requirement for the logistical expense of wide-angle acquisition.

To quantify the improvements that joint inversion makes over single inversion, we evaluate the performance of the inversion scheme in two ways. To indicate precision, we use the normalized interquartile range (i.e., half of the interquartile range as a percentage of the median)—δ_Z or δ_σ, for Z and σ, respectively. To indicate accuracy, we use the relative error (i.e., the difference between the median and true solution, as a percentage of the true solution)—ε_Z or ε_σ. The average is the median of the five results. Superscripts P and J indicate PP and joint inversion, respectively, and a superscript 30 or 60 indicates the angular range of the data. These metrics are displayed in Figure 4 for all of the tested bed types. Single (PP) inversion results are shown in blue; joint (PP/PS) inversion results are in red. Narrow survey geometries ($\theta \leq 30°$) are represented by the darker bars, with lighter bars representing wide survey geometries ($\theta \leq 60°$ or $\theta < \theta_{\text{crit}}$). In almost all cases, given the same angular range, jointly inverting PP and PS-waves improves both the accuracy and precision of the inversion when compared with inverting PP-waves only. In general, results from narrow joint inversion over $\theta \leq 30°$ compare favorably with wide single inversion over $\theta \leq 60°$.

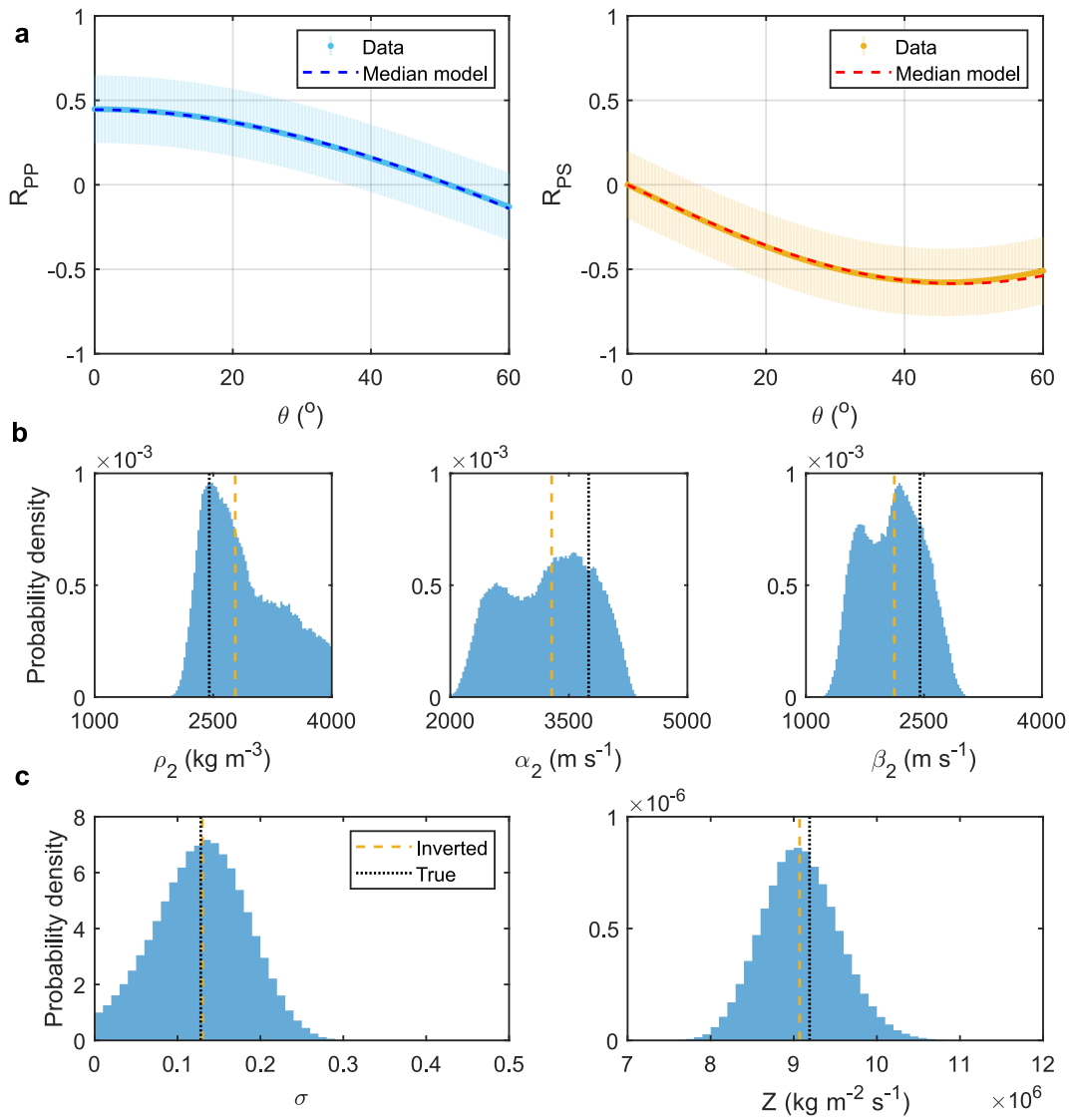

Figure 2. (a) Synthetic AVA responses used as inputs to an inversion, simulated for ice overlying lithified sediments (see Table 1 for properties). The dashed lines are the AVA responses of the median model. (b) Marginal distributions of density, P-wave velocity and S-wave velocity for the bed $(\rho_2, \alpha_2, \beta_2)$. (c) Marginal distributions of basal Poisson's ratio (σ) and acoustic impedance (Z). The medians of these distributions, along with the 25th and 75th percentiles, are the most representative quantities for interpretative purposes. In (b) and (c), black dotted lines indicate the model value and yellow dashed lines indicate distribution medians.

Joint inversion improves δ_Z over single inversion (Figure 4a), and is more precise given the same angular range of data: for all bed types δ_Z^J/δ_Z^P has a median of 0.77, and $\delta_\sigma^J/\delta_\sigma^P$ has median 0.55.

Furthermore, narrow joint inversion performs with comparable or slightly improved precision than wide single inversion: $\delta_Z^{P,30}/\delta_Z^{J,30}$ has median 0.9 across all bed types, and $\delta_\sigma^{J,30}/\delta_\sigma^{P,60}$ has median 0.86. The degree of improvement in δ_σ by joint inversion is largest for materials with high Poisson's ratios (Figure 4b): for both dilatant till and water, joint inversion reduces δ_σ from $\delta_\sigma^{P,30} > 10\%$ to $\delta_\sigma^{J,30} < 1\%$.

In general, accuracy is improved in both Z and σ by joint inversion (Figures 4c and 4d); however, the improvement in accuracy from joint inversion depends more strongly on the character of the subglacial material than the precision does. Joint inversion is in most cases more accurate than single inversion given the same angular range; $\epsilon_Z^J/\epsilon_Z^P$ has a median of 0.28, and $\epsilon_\sigma^J/\epsilon_\sigma^P$ has a median of 0.24, across all bed types tested. This

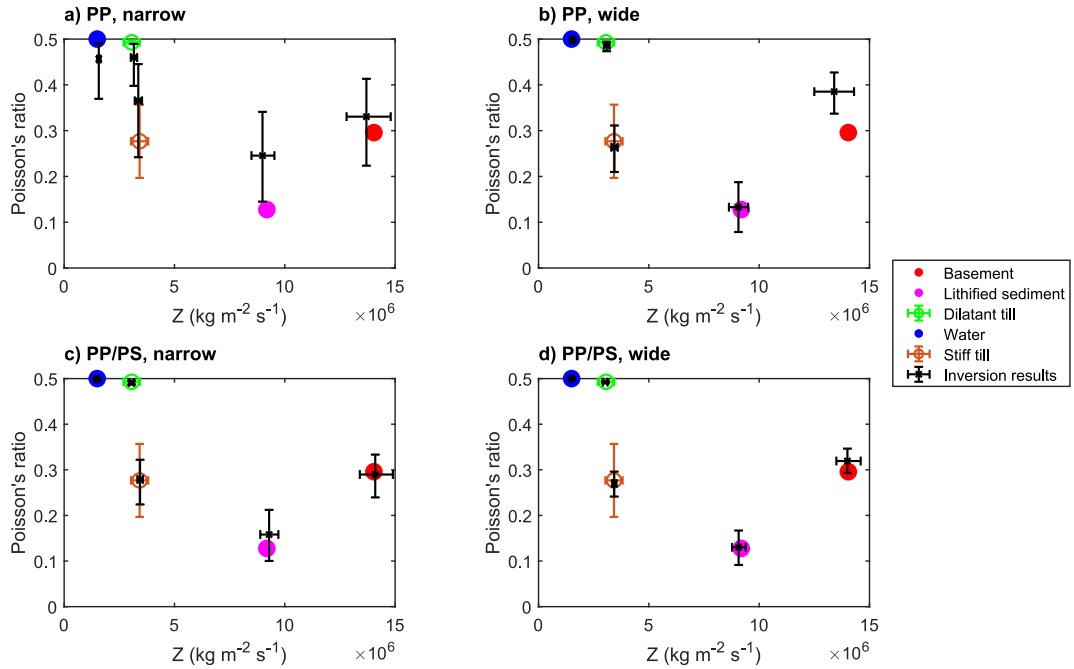

Figure 3. Results from synthetic PP and PP/PS joint inversions. Black crosses and error bars show inverted results. (a) and (b) show results for single PP inversion, and (c) and (d) show results from joint PP/PS inversion. Plots on the left (a, c) show the results from the narrow survey, where $\theta < 30°$, and plots on the right (b, d) show results from the wide survey, where $\theta < 60°$ (or $\theta < \theta_{crit}$). (b) and (c) demonstrate that joint inversion of narrow-angle data can deliver results of comparable precision and accuracy to single inversion of wide-angle data.

improvement is particularly pronounced for narrow inversions: $\varepsilon_Z^{J,30}/\varepsilon_Z^{P,30}$ has a median of 0.16 and $\varepsilon_\sigma^{J,30}/\varepsilon_\sigma^{P,30}$ has a median of 0.05 across all bed types. In general, narrow joint inversion is also more accurate than wide single inversion, for both Z and σ: $\varepsilon_Z^{J,30}/\varepsilon_Z^{P,60}$ has a median of 0.34 and $\varepsilon_\sigma^{J,30}/\varepsilon_\sigma^{P,30}$ has a median of 0.44 across all bed types.

In summary, joint inversion typically improves both precision and accuracy over single inversion. Furthermore, single wide-angle inversion and joint narrow-angle inversion produce comparable results. It is optimal to jointly invert all available PP/PS data over as wide an angle as possible. At some sites (e.g., where ice is very thick) acquiring three-component data may be easier than performing a wide-angle survey because of the larger offsets which must be reached. Experiments which include three-component recording for complementary reasons such as the measurement of crystal orientation fabric by shear-wave splitting (e.g., Brisbourne et al., 2019) will benefit from the potential to do converted-wave AVA with little extra logistical effort required. However, the degree of improvement of joint inversion over single inversion is highly sensitive to the substrate: if there are subglacial fluids present, wide-angle and converted-wave data improve inversions to similar extents. If a hard bed is present (basement, lithified or stiff sediments), both converted waves and wide angle data improve inversions less than for soft beds (dilatant till or water), because hard beds can be more confidently identified using the acoustic impedance alone.

3.4. Synthetic Seismic Example and Angle Sensitivity

To demonstrate the performance of the inversion on an example of synthetic seismic data with a realistic acquisition geometry and further illustrate the angle-dependence of the results, we generate synthetic seismograms using SPECFEM2D 8.1.0 (Komatitsch et al., 2023; Tromp et al., 2008), published under the GPL3 license. We generate one second of the seismic record for vertical and radial components, for a source buried at 40 m depth, with receivers at 10 m intervals between 30 and 1,940 m. We model 900 m thick ice underlain by dilatant till, with the velocity model in the firn taken from Brisbourne et al. (2019). This results in maximum incidence angles at the bed of 48° for PP reflections and 59° for PS. Frequency-wavenumber filters were applied to synthetic shot gathers to minimize interference from direct and surface waves. Vertical and radial components of synthetic

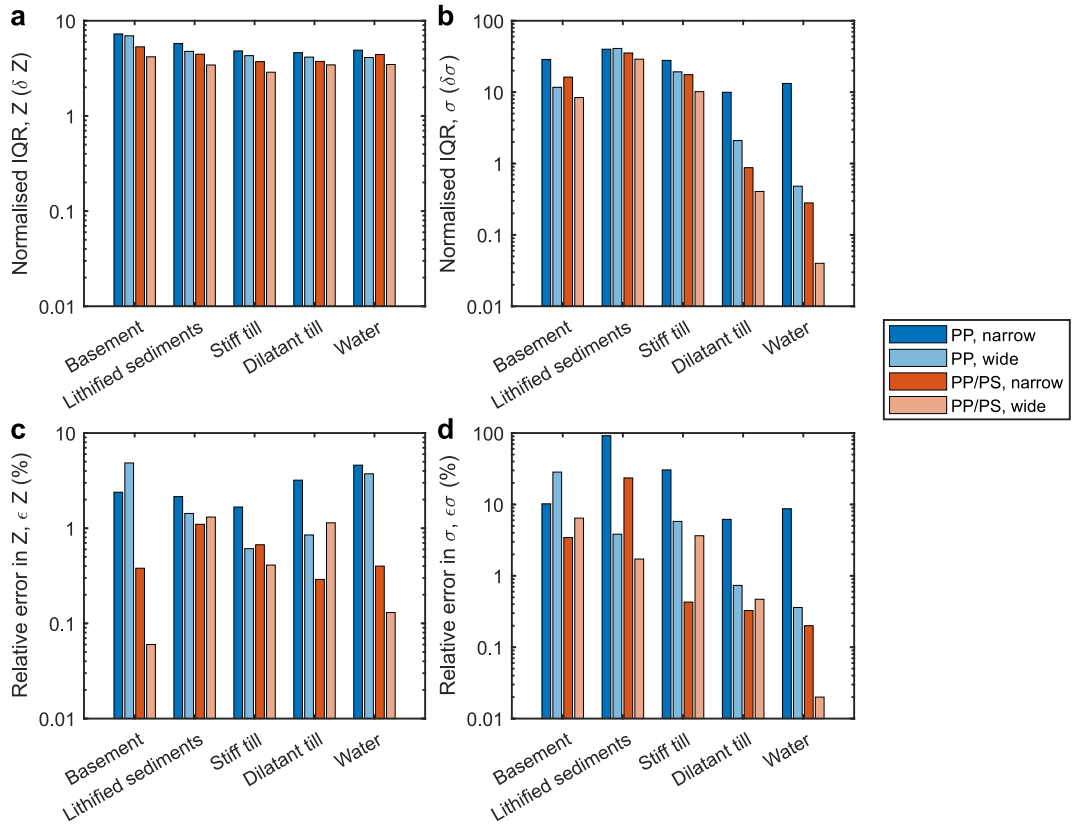

Figure 4. Normalized interquartile ranges of posterior distributions (a, b), and the relative error in the median of Z and σ (c, d). Note the logarithmic scales and different scales for acoustic impedance (Z) and Poisson's ratio (σ) plots.

shot gathers are shown in Figures 5a and 5b. Figure 5c shows AVA responses corrected for source amplitude, geometric and attenuation losses, grouped into bins of 1°, with error bars taken as the standard deviation in each bin. We run multiple single and joint inversions as described in the previous section, truncating the AVA responses in Figure 5c at successive intervals of 5° to test the angle sensitivity. We quantify the performance of the inversion as before, with the normalized interquartile ranges δ_Z, δ_σ (Figure 6a), and the relative errors ϵ_Z, ϵ_σ (Figure 6b). For both single and joint inversions, when the full AVA responses are used, δ_Z, δ_σ, ϵ_Z and ϵ_σ are close to or smaller than 5%, demonstrating the inversion scheme's effectiveness in retrieving basal properties from synthetic shot gathers.

For a given truncation angle $\theta_{\max}$, joint inversion is always more precise than single inversion in both Z and σ (Figure 6a), with the difference being particularly pronounced for δ_σ. The precision of Z is relatively insensitive to $\theta_{\max}$, reducing from $\delta_Z^{P,10} = \delta_Z^{J,10} = 9\%$ to $\delta_Z^{P,45} = 6\%$ and $\delta_Z^{J,45} = 4\%$. In contrast, precision in σ is sensitive to $\theta_{\max}$, with single and joint inversions being sensitive to $\theta_{\max}$ in different ranges. For PP inversions, δ_σ^P is insensitive to $\theta_{\max}$ at $\theta_{\max} < 25°$, whereafter δ_σ^P decreases rapidly, approaching δ_σ^J at $\theta_{\max} = 45°$, although even at large $\theta_{\max}$ joint inversion outperforms single inversion. For joint inversions, δ_σ^J shows its most rapid decrease between $\theta_{\max} = 10°$ and $\theta_{\max} = 20°$. These trends are also borne out in the inversion precision (Figure 6b). For both single and joint inversion, ϵ_Z^P and ϵ_Z^J are relatively insensitive to $\theta_{\max}$, with ϵ_Z^J consistently smaller than ϵ_Z^P. ϵ_σ^P decreases slowly with $\theta_{\max}$ from $10° \le \theta_{\max} \le 25°$, whereafter it decreases rapidly. This dramatic improvement coincides with the polarity reversal in the PP AVA response. ϵ_σ^J shows a decrease between $10° \le \theta_{\max} \le 20°$, whereafter it increases very slowly (this increase in ϵ_σ^J at larger angles may be a result of residual groundroll interference).

Single inversion achieves δ_Z, δ_σ, ϵ_Z and ϵ_σ of <10% at $\theta_{\max} \ge 35°$. Joint inversion achieves comparable results at $\theta_{\max} \ge 15°$. These results suggest that, at least for sites with basal dilatant sediment, reaching $\theta_{\max} > 35°–40°$ or

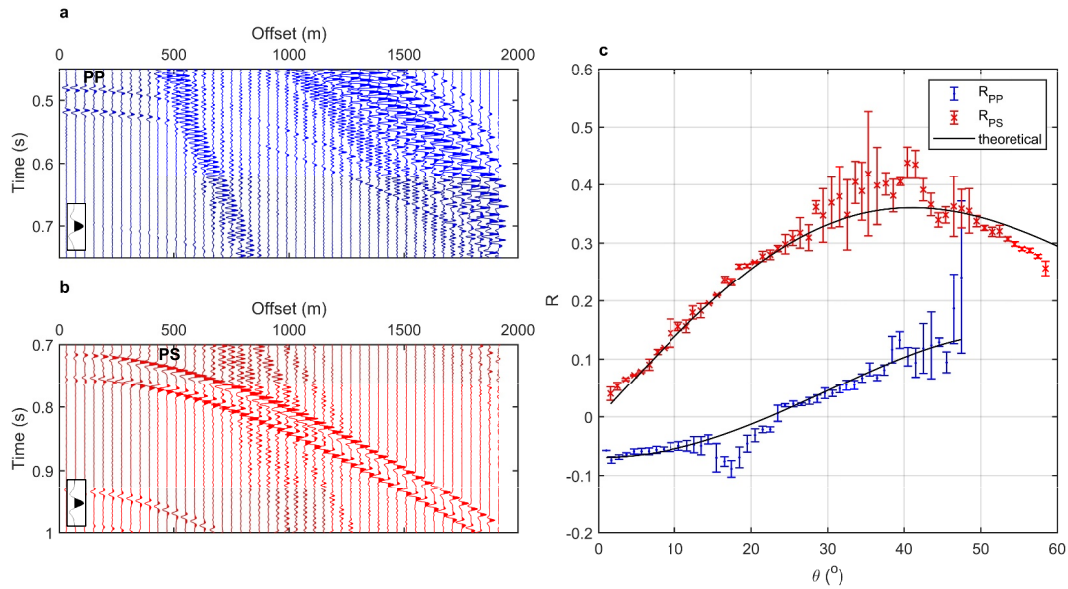

Figure 5. (a) Vertical component of synthetic shot gather focused on PP reflection, with source ghost closely following. Polarity reversal is visible at 750 m offset. (b) Radial component of synthetic shot gather focused on PS reflection. (c) AVA responses for PP and PS reflections, corrected for synthetic source amplitude, geometric spreading and attenuation losses. AVA data are binned into 1° intervals, with error bars given as the standard deviation in each bin. Black solid line is the theoretical reflectivity of input properties (Table 1). Inset boxes in (a) and (b) show the polarity of the direct wave.

capturing a polarity reversal is key to a satisfactory PP inversion, after which increases in $\theta_{\max}$ produce less dramatic improvements. Joint inversion of surveys which include acquisition of converted waves will improve on single-component surveys to the greatest extent when $\theta_{\max}^{PP} < 30°$. Capturing a PP polarity reversal does not appear to have a significant effect on the performance of a joint inversion, in contrast to single inversion. This may make joint inversions more robust to AVA responses of unknown substrates, where the angle of polarity reversal may not be predicted in advance.

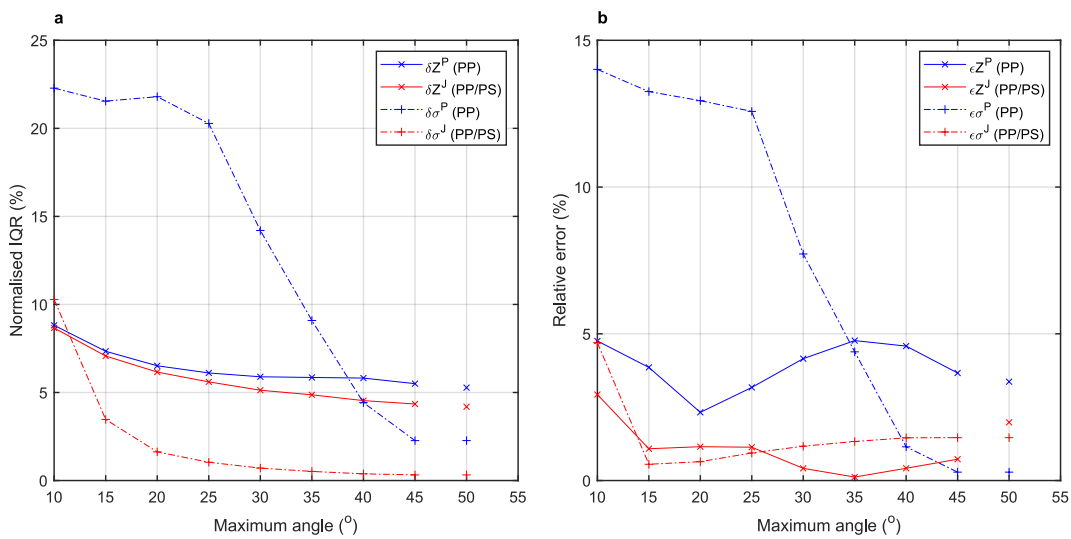

Figure 6. Performance of inversion scheme on synthetic seismic gather, for a dilatant sediment bed. (a) Normalized IQR in acoustic impedance (δ_Z) and Poisson's ratio (δ_σ) versus maximum angle for single (PP) and joint (PP/PS) inversions. (b) Relative error in acoustic impedance (ϵ_Z) and Poisson's ratio (ϵ_σ) for single and joint inversions. Separated points shown at 50° are results from inversion of the greatest extent of data available ($\theta_{\max} = 48°$ for PP and $\theta_{\max} = 59°$ for PS reflections).

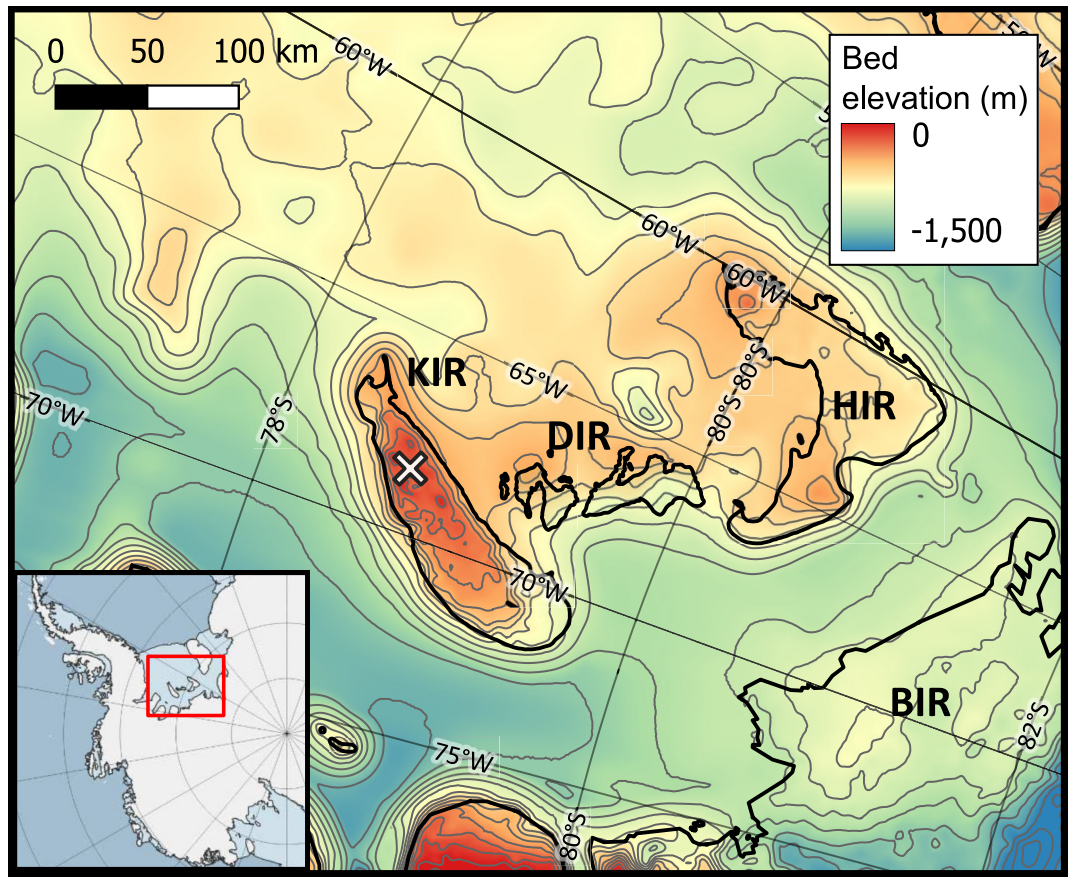

Figure 7. Subglacial topography in the region surrounding Korff Ice Rise (KIR), from Bedmap2 (Fretwell et al., 2013). Field site is marked with the white cross. Inset shows location within Antarctica. HIR = Henry Ice Rise, BIR = Bungenstock Ice Rise, DIR = Doake Ice Rumples.

4. Joint AVA Inversion of PP and PS Reflection Amplitudes at Korff Ice Rise

4.1. Korff Ice Rise

Korff Ice Rise (KIR), in the Ronne Ice Shelf in the Weddell Sea Sector, West Antarctica, has an ice thickness of ~530 m at its northern end (Figure 7). KIR is situated in a group of ice rises and rumples which occupy an area of higher seabed elevation between bathymetric troughs, and includes the Doake Ice Rumples (DIR) and Henry Ice Rise (HIR). While the extent of the grounded ice sheet at the last glacial maximum (LGM) is well understood (Bentley et al., 2014), consensus has yet to be reached on the evolution of the grounding line from its LGM extent to its present position. Some authors have proposed monotonic retreat of the grounding line to its present day position after the LGM (Hillenbrand et al., 2014), with others proposing rapid grounding line retreat to a position inland of the current grounding line, followed by a readvance of the grounding line to its present day position (Bradley et al., 2015; Kingslake et al., 2018). This readvance has been hypothesized to result from glacial isostatic adjustment (Kingslake et al., 2018) or climatic and oceanographic forcings (Neuhaus et al., 2021). These ice rises may have partially or completely ungrounded and subsequently regrounded during retreat/readvance. Holocene flow reorganization at KIR has been inferred from englacial layering (Kingslake et al., 2016) and crystal orientation fabric (Brisbourne et al., 2019), and there is evidence for ungrounding and regrounding at Henry Ice Rise (Wearing & Kingslake, 2019). Observations of basal properties at KIR may enhance the understanding of the ice flow history in this region. Given the slow ice flow and shape of the surface topography, KIR is hypothesized to be presently cold-based with the ice frozen to the bed.

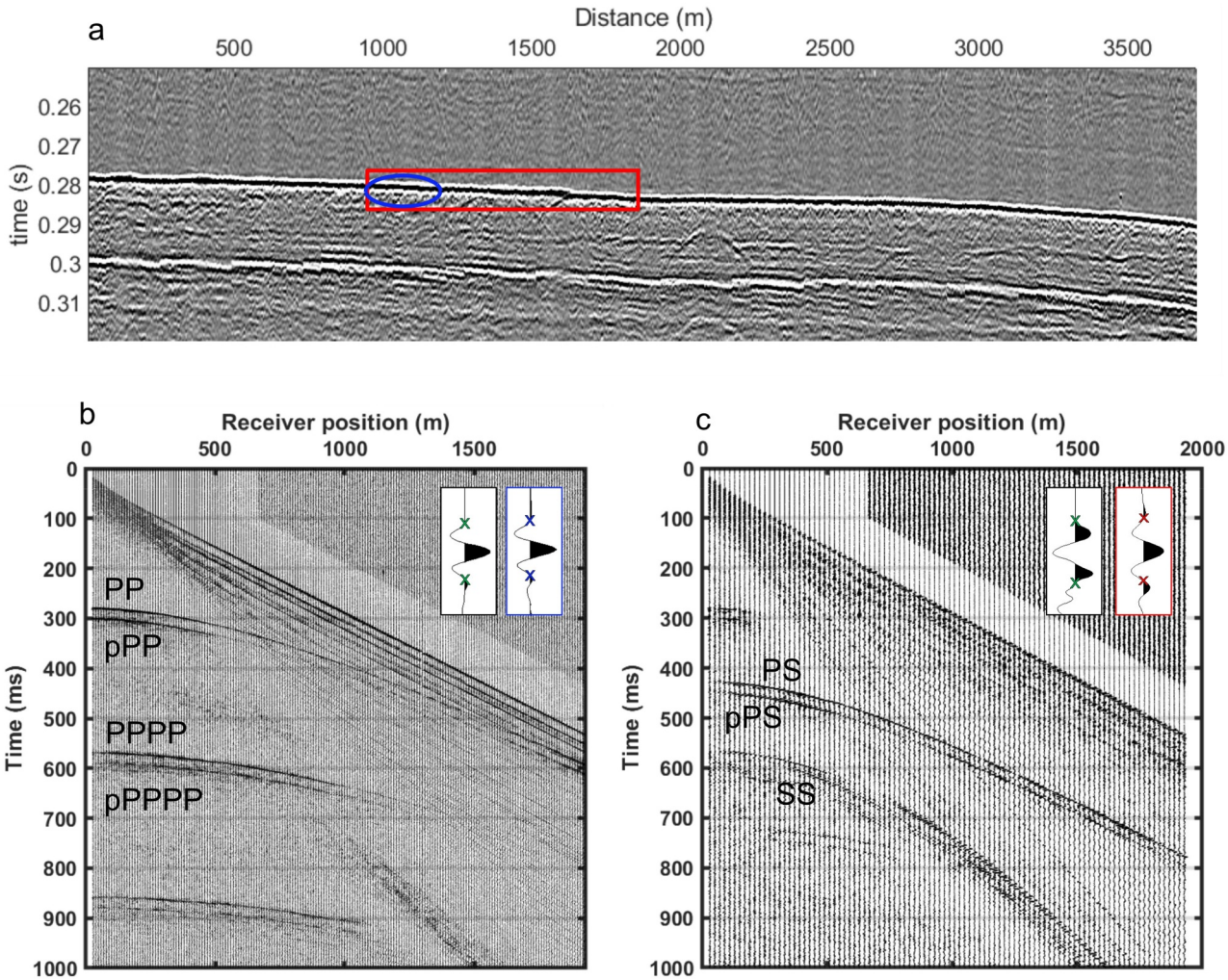

Figure 8. (a) Unmigrated time section along the divide axis, highlighting the range of AVA reflection points for PP-waves (blue) and PS-waves (red). The event at 0.28 s is the PP basal reflection, and that at 0.3 s is its source ghost, pPP. (b) Data recorded in acquisition i identifying primary (PP) and first multiple (PPPP) bed reflections, and corresponding source ghosts (pPP, pPPPP). (c) Radial component data recorded in acquisition ii identifying converted (PS) and shear-wave (SS) reflections, and corresponding source ghost (pPS). Insets in (b) and (c) show wavelets of the diving waves (black outline, left), and PP and PS reflections (blue = PP, red = PS), illustrating the polarity convention. PP is positive polarity and PS negative. Note polarity convention is opposite for vertical and radial components. Wavelets are extracted between the second zero crossings ("x" symbols) either side of the wavelet maximum. Data in (b) and (c) have automatic gain control applied (window length: 200 ms) for display purposes.

4.2. Data

In the austral summer season of 2014/15, seismic surveys were carried out at KIR to investigate the location as a potential site for ice coring. Data were acquired along a line parallel to the ice divide. Prior to the AVA experiments, a 4km long seismic reflection profile was acquired along the divide, with 48 × 40 Hz Georods (Voigt et al., 2013) deployed at 10 m intervals. Shots were alternately 30 m offset from channel 1 and at channel 10 within the georod spread, with 150 g Pentolite sources at 20 m depth. Figure 8a shows the normal-moveout corrected unmigrated time section. The ice-base interface appears as a well-defined positive polarity wavelet.

AVA data were acquired from a line of vertically oriented georods at 10 m intervals, installed between 30 and 1,940 m offset, with a 150 g Pentolite source buried in 20 m deep boreholes. These data were recorded with an 8 kHz sampling rate (Acquisition i). We use these data for the P-wave AVA measurements. Four separate shots were recorded in a walkaway survey, which are combined into the supergather shown in Figure 8b. Nominal bounce points for PP and PS basal reflections are shown in Figure 8a. The first Fresnel radius at normal incidence is less than 80 m.

To record shear waves, data were recorded in a second acquisition (Acquisition ii). To produce shear waves, a 600 g Pentolite source was used, buried at 20 m depth. A larger charge size was found to be necessary to produce sufficient amplitudes of shear waves from mode conversions near to the source. Georods were installed at 10 m intervals, between 30 and 1,940 m offset, alternating between radial and transverse orientations. Data were recorded with 8 kHz sampling rate. Again, four separate shots were recorded in a walkaway survey and combined into a supergather, the radial component of which is shown in Figure 8b. Surface source data were acquired to constrain near-surface velocities and attenuation (Agnew et al., 2023). Amplitudes of reflected and diving waves are measured as the root-mean-square of the wavelet (minimum phase), picked between the second zero crossings either side of the wavelet maximum (e.g., Horgan et al., 2021). Wavelets are picked on raw shot gathers with no preprocessing.

4.3. AVA Processing

4.3.1. Velocity Model, Geometric and Attenuation Corrections

Wiechert-Herglotz inversion of diving wave travel times was used to obtain near-surface P and S-wave velocities (using the method by Kirchner & Bentley, 1979). We assume a linearly increasing temperature profile from the surface to the bed (e.g., Mulvaney et al., 2021) and calculate velocities from Kohnen's empirical relation (Kohnen, 1972), tuning velocities to match normal-incidence arrival times (Brisbourne et al., 2023). We assume spherical spreading inversely proportional to the path length r, and correct for the incidence angle of the ray at the receiver (e.g., Zechmann et al., 2018). The correction factor $\gamma(x)$ for P-waves of path length $r(x)$ arriving at an angle θ_{rec} to the vertical is

$$\gamma(x) = \frac{1}{r(x)} \cos\theta_{\text{rec}}. \tag{9}$$

We use $Q_P = 250 \pm 100$ for the whole ice column (Agnew et al., 2023) and assume $Q_P/Q_S = 3$ (Clee et al., 1969), that is, $Q_S = 83 \pm 30$. For the PP reflection, we correct amplitudes for a single frequency of $f = 300$ Hz, and for PS, we correct for a single frequency $f = 225$ Hz. These frequencies were determined by inspection of reflected wavelet spectra.

4.3.2. Source Amplitude

The PP and PS reflections were recorded using different sized charges, so the source amplitude must be independently constrained for each acquisition. Amplitudes were adjusted to ensure continuity of diving wave amplitudes between shots for each acquisition. To estimate the source amplitude of the PP reflection (Acquisition i), we use the multiple-bounce method, which compares the amplitudes A_1 and A_2 of the primary reflection and its first multiple at normal incidence:

$$A_{0,PP} = \frac{{A_1}^2}{A_2} \frac{1}{2\gamma_1}, \tag{10}$$

where γ_1 is the geometric correction for the primary reflection (Holland & Anandakrishnan, 2009). The source amplitude for the PP reflection recorded in Acquisition i was measured as $(2.22 \pm 1) \times 10^8$ counts.

Acquisition ii included no vertically oriented georods, so the P-wave first-order multiple (PPPP) was not recorded. Consequently, we measure the source amplitude for Acquisition ii using diving P-waves measured on radial component georods (Holland & Anandakrishnan, 2009). Prior to the measurement of source amplitude, amplitudes were corrected for incidence angle at the receiver θ_{rec} using

$$A = \frac{A_r}{\sin\theta_{\text{rec}}}. \tag{11}$$

A is the true amplitude of the diving P-wave and A_r its component of amplitude measured by a radial georod.

4.3.2.1. Variable-Q Direct-Path Method

The direct-path method by Holland and Anandakrishnan (2009) has been used by previous workers to estimate source amplitude $A_{0,\text{direct}}$ when multiples have not been recorded (e.g., Clyne et al., 2020; Muto et al., 2019). It uses the amplitudes B_1 and B_2 of two diving waves with path lengths r_1, r_2 and geometric spreading factors γ_1, γ_2, which are chosen such that $r_2/r_1 \simeq 2$:

$$A_{0,\text{direct}} = \frac{{B_1}^2}{B_2}\frac{\gamma_2}{{\gamma_1}^2}. \tag{12}$$

Equation 12 assumes that the path-integrated attenuation is the same for the two diving ray paths. However, recent work has shown that in firn, the seismic quality factor Q increases with depth (Agnew et al., 2023; Picotti et al., 2024). As source-receiver offset increases, diving waves penetrate deeper into the firn, and the path-integrated Q of the rays, Q_{path}, increases. Near to the base of the firn, the velocity increases slowly with depth: for two rays propagating here, a far offset ray may emerge at a much greater offset while only penetrating slightly deeper than a near-offset ray. The depth-integrated Q_{depth} is similar for the two rays, but the path-integrated Q_{path} for the further offset ray is larger, since this ray spends a greater proportion of its total propagation time in the higher-Q deep firn. Consequently $A_{0,\text{direct}}$ is an underestimate of source amplitude. To estimate the Q-corrected source amplitude, $A_{0,\text{vQ}}$, Equation 12 can be modified with an exponential term:

$$A_{0,\text{vQ}} = \frac{{B_1}^2}{B_2}\frac{\gamma_2}{{\gamma_1}^2}e^{\pi f\left(2t_1^* - t_2^*\right)}, \tag{13}$$

where f is the frequency of the diving wave and t_1^*, t_2^* are the attenuated times of rays 1 and 2, respectively. Where $r_2 = 2r_1$, the geometric spreading terms reduce to $\gamma_2/\gamma_1^2 = r_1/2$. We call this method the variable-Q direct-path method.

We estimate A_0 using pairs of rays at offsets x_1, x_2 with path lengths r_1, r_2 for which $1.995 < \frac{r_1}{r_2} < 2.005$ and $x_1 > 500$ m. For all offset pairs, both rays penetrate close to the base of the firn column. Rays are traced to estimate t^* for each ray at a single frequency of $f = 300$ Hz. We compute A_0 using the two methods, using the same rays. Using the conventional direct-path method, the source amplitude is $A_{0,\text{direct}} = (2.6 \pm 1.9) \times 10^8$ counts. The variable-Q direct-path method, using a Q-vs-depth model previously derived at this location (Agnew et al., 2023), results in a corrected source amplitude of $A_{0,\text{vQ}} = (4.1 \pm 2.9) \times 10^8$ counts, meaning that Equation 12 underestimates A_0 by a factor of ~ 1.6. Using $A_{0,\text{direct}}$ would overestimate reflectivities by the same factor. For further analysis we use $A_{0,\text{PS}} = A_{0,\text{vQ}} = (4.1 \pm 2.9) \times 10^8$ counts for the source amplitude of the PS-wave.

4.4. AVA Responses and Inversion Setup

Using Equation 2 for PP amplitudes and Equation 5 for PS amplitudes, the PP and PS AVA responses were corrected for source amplitude, geometric spreading and attenuation terms; the corrected AVA responses are shown in Figure 9. Incidence angles, obtained by ray tracing, reach 63° for PP and 73° for PS reflections. R_{PP} decreases from 0.15 ± 0.1 at close to normal incidence to 0.03 ± 0.03 at 57°, before rising again. R_{PS} has its greatest magnitude of -0.6 ± 0.7 at 45°. To explore the joint inversion's performance on these real data, we run four separate inversions of the AVA responses, which invert different subsets of the available data: (a) the PP response only, with data for $0 \le \theta \le 30°$ only (56 data points); (b) PP and PS, over $0 \le \theta \le 30°$ (76 data points); (c) PP only, using wide-angle data ($\theta \le 63°$, 192 data points); and (d) PP and PS, using wide-angle data ($\theta_{PP} \le 63°, \theta_{PS} \le 73°$, 288 data points). We run each inversion for 5,000,000 iterations. We run each inversion repeatedly from different starting points to confirm convergence. The basal ice properties are assumed in the prior to be $\alpha_{\text{ice}} = 3830 \pm 50$ m s^{-1}, $\beta_{\text{ice}} = 1906 \pm 50$ m s^{-1}, and $\rho_{\text{ice}} = 920 \pm 50$ kg m^{-3}. The solid lines shown in Figure 9 represent the median model found by jointly inverting R_{PP} and R_{PS} using wide-angle data (our best estimate). The AVA response implied by this model shows a critical refraction at 72°, consistent with the observed rise in R_{PP} toward 70°.

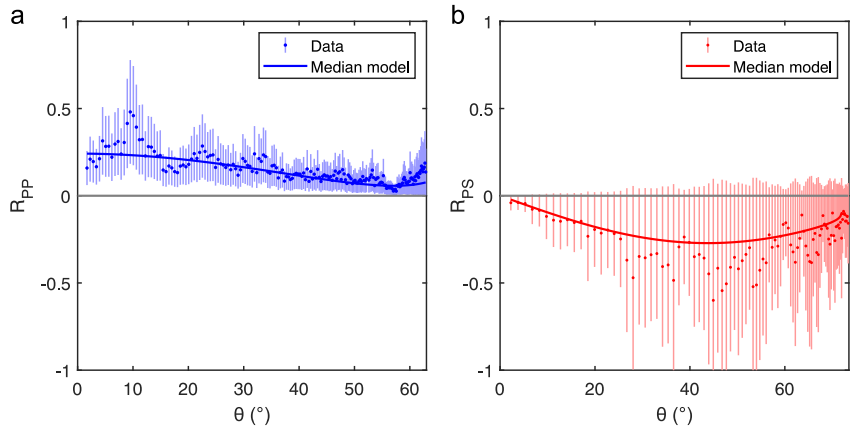

Figure 9. (a) PP, and (b) PS AVA responses at Korff Ice Rise. Solid lines indicate median models from jointly inverting wide-angle data. Cyclical amplitude variations are assumed to result from inhomogeneities in basal properties between Fresnel zones across the area of reflections.

4.5. AVA Results

Results of the four inversions are summarized in Figure 10, which shows marginal distributions of Z and σ. An expanded list of inverted properties for these four cases is given in Table B1, which quotes the medians and interquartile ranges of output marginal distributions, as well as the normalized interquartile ranges εZ and $\varepsilon\sigma$. For the 0–30° inversions (Figures 10a and 10c), Z is well constrained but σ is not. Joint inversion offers a marginal improvement over single inversion, with the ratio of normalized interquartile ranges for both Z and σ close to 0.9: $\varepsilon Z^{J,30}/\varepsilon Z^{P,30} = 0.88$ and $\varepsilon\sigma^{J,30}/\varepsilon\sigma^{P,30} = 0.86$.

When wide-angle data were used, both Z and σ were better constrained than in the restricted angle case, for single and joint inversion, but the improvement in constraint of Z was small. There is no improvement in constraint of Z when comparing wide-angle joint inversion with wide-angle single inversion: $Z^{J,\text{wide}} = (5.79 \pm 0.26) \times 10^6$ kg m^{-2}s^{-1} versus. $Z^{P,\text{wide}} = (5.69 \pm 0.26) \times 10^6$ kg m^{-2}s^{-1}. The ratio of normalized interquartile ranges is $\varepsilon Z^{J,\text{wide}}/\varepsilon Z^{P,\text{wide}} = 0.98$. While extending the inversion to wide angles did not improve constraint of Z, it did improve constraint of σ: the ratio of normalized uncertainties for joint inversion is $\varepsilon\sigma^{J,\text{wide}}/\varepsilon\sigma^{J,30} = 0.15$; for single inversion, $\varepsilon\sigma^{P,\text{wide}}/\varepsilon\sigma^{P,30} = 0.19$. For this data set, the wide-angle data are more valuable than the converted-wave data.

All four inversions result in consistent basal properties. For our best estimate of basal properties, we take the best-constrained result from joint inversion of wide-angle data due to the slight improvement over single inversion: $Z = Z^{J,\text{all}} = (5.79 \pm 0.26) \times 10^6$ kg m^{-2}s^{-1} and $\sigma = \sigma^{J,\text{all}} = 0.298 \pm 0.010$.

5. Discussion

5.1. Basal Conditions at KIR

The acoustic impedance and Poisson's ratio of the basal material at KIR suggest a bed composed of partially consolidated and/or frozen sediments. The acoustic impedance indicates a relatively stiff material; the Poisson's ratio, close to that of ice ($\sigma_{\text{ice}} = 0.34$), is consistent with a reflection from ice over a frozen sedimentary bed, where the pore space is occupied mainly or completely by ice. This inference of a frozen bed is consistent with both monotonic retreat (with a previous phase of ice sheet flow over a warm bed), and a rapid retreat/readvance scenario including ungrounding (where the current subglacial material may consist of what were previously water-saturated marine sediments). The seismic observations described in the previous section do not allow us to discriminate between these scenarios.

Thin layering (Booth et al., 2012) or the presence of debris at the ice-bed interface (Chandra et al., 2025) can alter reflectivities and the results of AVA inversions. It is worth considering if a thin layer response from a warm bed may be consistent with the observed reflectivity, as this would signal anomalously high geothermal heat flux or very recent grounding. If the present regime was preceded by an ice shelf over glaciomarine sediments, shortly

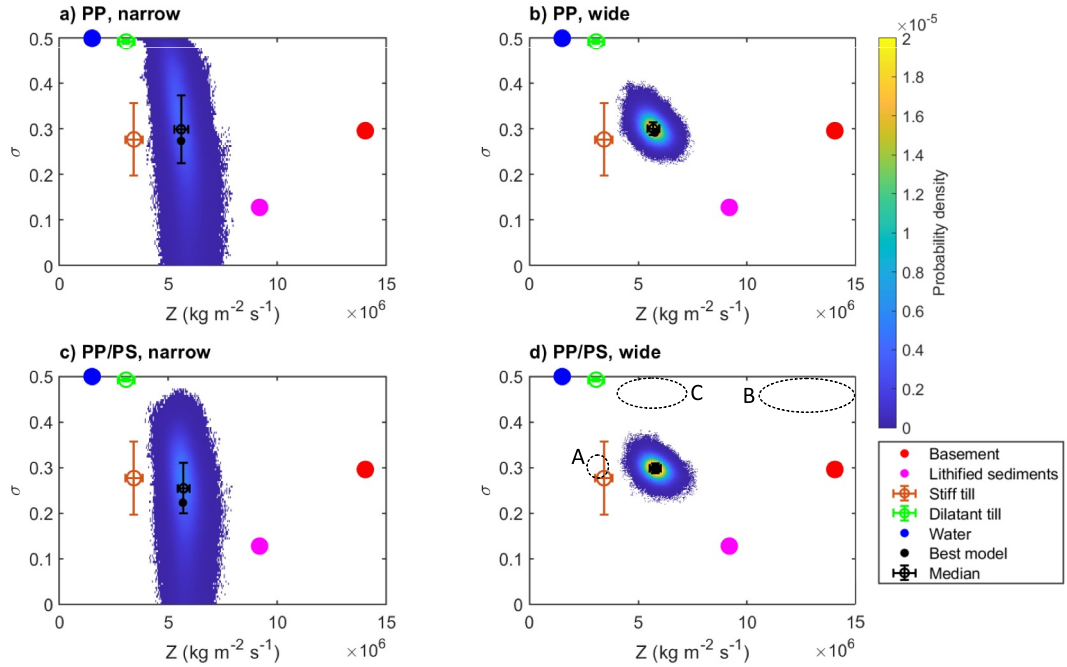

Figure 10. Inverted bed properties at Korff Ice Rise. (a) PP-only inversion, using $\theta \leq 30°$. (b) PP-only inversion, using wide-angle data. (c) Joint PP/PS inversion, using $\theta \leq 30°$. (d) Joint PP/PS inversion, using wide-angle ($\theta_{PP} \leq 63°, \theta_{PS} \leq 73°$) data. Ellipses marked A, B and C refer to hypothetical thin-layer scenarios discussed in Section 5.1, which are inconsistent with the data.

after grounding, water or brine would occupy the pore space immediately under the ice base. Booth et al. (2012) interpret that in a thin layer AVA response arising from three layers at the ice-bed interface (e.g., ice - dilatant till - lodged till), the apparent acoustic impedance of the glacier bed is dominated by the acoustic impedance of the underlying "thick" layer and the apparent Poisson's ratio is dominated by the Poisson's ratio of the "thin" layer. If there were a thin layer of debris-rich basal ice overlying water or brine saturated sediments, we would likely observe an apparent acoustic impedance in the region of 3×10^6 kg m^{-2}s^{-1} (hypothetical scenario A, marked on Figure 10d with a dashed ellipse), which is inconsistent with the observations at KIR. Another plausible thin layer scenario for a warm bed would be that of a thin layer composed of ice, brine and debris, overlying a bed of crystalline bedrock (scenario B, marked on Figure 10d) or stiff sediments (scenario C, marked on Figure 10d). Our inverted acoustic impedance is too low to accommodate bedrock underneath the basal ice, so this is excluded. We do, however, observe an acoustic impedance plausible in consolidated sediments. If the bed were warm enough to accommodate significant basal melting, the basal debris layer would likely not be fully frozen, but would be a mixture of ice, debris and water. The apparent Poisson's ratio would likely be higher than we observe due to the liquid in the thin layer. This is inconsistent with our observations. Therefore, we consider the AVA inversions presented above as strong evidence for a frozen bed at KIR. This is in agreement with studies which model KIR to be frozen at the base (Dawson et al., 2022).

5.2. Implications for Future Data Acquisition

Given finite logistical constraints, is it preferable to do a wide-angle survey or a three-component narrow-angle survey? The synthetic results suggest that if no prior information was available about the substrate, it may be preferable to expend logistical resources acquiring three-component data. However, as the data set presented here demonstrates, there exist glaciological scenarios for which obtaining wide-angle data improves constraint of bed properties more than three-component analysis does. This is consistent with the synthetic experiments, which indicate that converted-wave acquisition and joint inversion are most advantageous if the expected subglacial material has a high Poisson's ratio. More three-component AVA data sets must be acquired in diverse glacial environments to understand more fully the potential and limitations of converted wave joint inversion; as three-component recording becomes the norm, this will become clearer. We are therefore reluctant

at present to recommend exclusively sacrificing PP coverage for PS coverage if acquisition of wide-angle data is logistically feasible. Both wide-angle P-wave AVA responses and PS AVA responses are sensitive to the proportion of energy converted into transmitted and reflected P and S phases at the reflecting interface. Measurement of PS-waves at the ice surface, if undertaken in tandem with a wide-angle acquisition, provides a means to extend the coverage and quantity of data, but is fundamentally sensitive to the same properties at the ice-bed interface.

Acquisition of radial-component data need not always come at the expense of vertical-component data. When experiments plan to use equipment such as 3-component seismic nodes, joint inversion represents a way to maximize the value of an AVA data set. Furthermore, if a survey also aims to acquire data suitable for shear-wave splitting analysis as was the case for this data set (e.g., Brisbourne et al., 2019), designing a survey with converted wave analysis in mind need not be detrimental to vertical acquisition. If possible, future acquisitions should aim to record vertical and horizontal components from the same source, to avoid processing complexities and introduction of error associated with the measurement of source amplitude.

6. Conclusions

We have investigated the potential of seismic PP- and PS-wave joint inversion to improve upon conventional methods of AVA inversion. In general, converted-wave joint inversion improves upon PP-wave single inversion in both accuracy and precision. Joint inversion of AVA data with a maximum incidence angle of 30° performs similarly or favorably when compared with single inversion of data with incidence angles extending to 60°. The degree to which joint inversion is an improvement over single inversion, and the relative utility of three-component versus wide-angle data, is dependent on the character of the AVA response, so future surveys must be planned carefully to determine the optimal survey parameters for a particular glaciological target. Acquisition of converted wave data may be most beneficial when there is fluid present in the subglacial environment. Converted wave joint inversion may make acquisition of AVA data easier and maximize the utility of data which include 3-component recording for complementary reasons such as shear-wave splitting measurements. This has the potential to optimize planning in time sensitive field deployments.

We applied our joint inversion scheme to investigate the subglacial properties at Korff Ice Rise (KIR), an ice rise in the Weddell Sea sector of West Antarctica. Using joint inversion, we find that the bed has an acoustic impedance of $Z = (5.79 \pm 0.26) \times 10^6$ kg m^{-2}s^{-1} and a Poisson's ratio of $\sigma = 0.298 \pm 0.010$. We interpret these properties as consistent with a frozen bed at KIR. For this data set, inclusion of wide-angle data constrains the inversion to a greater degree than inclusion of converted wave data. This is consistent with the synthetic results; however, this emphasizes the need for careful survey planning and consideration of the glaciological environment and likely basal properties when deciding whether to focus efforts on extending spatial coverage or acquiring multicomponent data.

Appendix A: Synthetic Results

Table A1
Results of Synthetic Tests

Basal material	Inversion type	Max angle (°)	Z true ($\times 10^6$ kg m^{-2}s^{-1})	σ true	Z inverted ($\times 10^6$ kg m^{-2}s^{-1})	σ inverted
Basement	PP	30	14.04	0.3	13.71 ± 1.00	0.331 ± 0.095
Basement	PP	46	14.04	0.3	13.36 ± 0.93	0.385 ± 0.045
Basement	PP/PS	30	14.04	0.3	14.09 ± 0.75	0.290 ± 0.047
Basement	PP/PS	46	14.04	0.3	14.03 ± 0.59	0.319 ± 0.027
Dilatant till	P	30	3.06	0.49	3.16 ± 0.15	0.460 ± 0.046
Dilatant till	P	60	3.06	0.49	3.09 ± 0.13	0.486 ± 0.010
Dilatant till	PP/PS	30	3.06	0.49	3.05 ± 0.11	0.492 ± 0.004
Dilatant till	PP/PS	60	3.06	0.49	3.03 ± 0.10	0.492 ± 0.002
Lithified sediments	P	30	9.19	0.128	8.99 ± 0.52	0.246 ± 0.098
Lithified sediments	P	60	9.19	0.128	9.06 ± 0.43	0.133 ± 0.054
Lithified sediments	PP/PS	30	9.19	0.128	9.29 ± 0.41	0.158 ± 0.056
Lithified sediments	PP/PS	60	9.19	0.128	9.07 ± 0.31	0.130 ± 0.038
Stiff till	P	30	3.42	0.28	3.36 ± 0.16	0.365 ± 0.102
Stiff till	P	60	3.42	0.28	3.44 ± 0.15	0.264 ± 0.051
Stiff till	PP/PS	30	3.42	0.28	3.44 ± 0.13	0.279 ± 0.049
Stiff till	PP/PS	60	3.42	0.28	3.43 ± 0.10	0.270 ± 0.027
Water	P	30	1.50	0.5	1.57 ± 0.08	0.457 ± 0.060
Water	P	60	1.50	0.5	1.56 ± 0.06	0.498 ± 0.002
Water	PP/PS	30	1.50	0.5	1.49 ± 0.07	0.499 ± 0.001
Water	PP/PS	60	1.50	0.5	1.50 ± 0.05	0.500 ± 0.0002

Note. Results comparing PP and PP/PS inversions are discussed in Section 3.3. Note an ice/basement reflection goes critical at 46°, hence the angles are limited.

Appendix B: Inverted Properties at KIR

Table B1
Results From All Inversions of Korff AVA Responses

Inversion type	Extent	Z ($\times 10^6$ kg m^{-2}s^{-1})	σ	εZ (%)	$\varepsilon\sigma$ (%)
PP	$\theta_{PP} \leq 30°$	5.59 ± 0.30	0.299 ± 0.075	5.4	25
PP/PS	$\theta_{PP,PS} \leq 30°$	5.69 ± 0.27	0.255 ± 0.055	4.8	22
PP	$\theta_{PP} \leq 63°$	5.69 ± 0.26	0.300 ± 0.014	4.6	4.7
PP/PS	$\theta_{PP} \leq 63°, \theta_{PS} \leq 73°,$	5.79 ± 0.26	0.298 ± 0.010	4.5	3.4

Note. All results quoted are medians ± interquartile range of marginal distributions.

Conflict of Interest

The authors declare no conflicts of interest relevant to this study.

Data Availability Statement

The synthetic AVA responses were generated using the CREWES MATLAB toolbox (Margrave & Lamoureux, 2019, available from https://www.crewes.org/ResearchLinks/FreeSoftware/www.crewes.org). MCMC

inversions were carried out in MATLAB. Code can be accessed at Zenodo (Agnew, 2025); https://doi.org/10.5281/zenodo.17901754.

Seismic data are available from the NERC UK Polar Data Centre. The AVA data are available at https://doi.org/10.5285/c563569e-0875-404b-acb2-cd5f9e5c4706 (Brisbourne & Smith, 2018). The reflection profile shot gathers are being archived with the NERC UK Polar Data Centre (Agnew et al., 2025): https://doi.org/10.5285/e9ed7128-eeed-4478-b308-8d1ea347dfa4.

Acknowledgments
These data were collected as part of the British Antarctic Survey programme Polar Science for Planet Earth with the support of British Antarctic Survey Operations. RSA was supported by the NERC PANORAMA Doctoral Training Partnership at the University of Leeds (Grant NE/S007458/1). We thank the editor and the two anonymous reviewers for their feedback which helped to improve the manuscript.

References

Agnew, R. S. (2025). AgnewR/mcmc-ava: mcmc-ava-v1.0.2 (mcmc-ava-v1.0.2). *Zenodo*. https://doi.org/10.5281/zenodo.17901754

Agnew, R. S., Brisbourne, A., & Smith, A. (2025). Seismic reflection and refraction shot gathers from Korff Ice Rise, West Antarctica, 2015 (version 1.0) [Dataset]. *NERC EDS UK Polar Data Centre*. https://doi.org/10.5285/e9ed7128-eeed-4478-b308-8d1ea347dfa4

Agnew, R. S., Clark, R. A., Booth, A. D., Brisbourne, A. M., & Smith, A. M. (2023). Measuring seismic attenuation in polar firn: Method and application to Korff Ice Rise, West Antarctica. *Journal of Glaciology*, *69*(278), 2075–2086. https://doi.org/10.1017/jog.2023.82

Agnew, R. S., Pearce, E., Karplus, M., Ranganathan, M., Hoffman, A. O., Hunt, M., et al. (2025). Active and passive seismic surveys over the grounding zone of Eastwind Glacier, Antarctica. *Seismological Research Letters*. https://doi.org/10.1785/0220250024

Anandakrishnan, S. (2003). Dilatant till layer near the onset of streaming flow of Ice Stream C, West Antarctica, determined by AVO (amplitude vs offset) analysis. *Annals of Glaciology*, *36*, 283–286. https://doi.org/10.3189/172756403781816329

Anandakrishnan, S., & Alley, R. B. (1997). Stagnation of Ice Stream C, West Antarctica by water piracy. *Geophysical Research Letters*, *24*(3), 265–268. https://doi.org/10.1029/96GL04016

Bentley, M. J., Ó Cofaigh, C., Anderson, J. B., Conway, H., Davies, B., Graham, A. G., et al. (2014). A community-based geological reconstruction of Antarctic Ice Sheet deglaciation since the last glacial maximum. *Quaternary Science Reviews*, *100*, 1–9. (Reconstruction of Antarctic Ice Sheet Deglaciation (RAISED)). https://doi.org/10.1016/j.quascirev.2014.06.025

Blankenship, D. D., Bentley, C. R., Rooney, S. T., & Alley, R. B. (1987). Till beneath ice stream B: 1. properties derived from seismic travel times. *Journal of Geophysical Research*, *92*(B9), 8903–8911. https://doi.org/10.1029/JB092iB09p08903

Booth, A. D., Clark, R. A., Kulessa, B., Murray, T., Carter, J., Doyle, S., & Hubbard, A. (2012). Thin-layer effects in glaciological seismic amplitude-versus-angle (AVA) analysis: Implications for characterising a subglacial till unit, Russell Glacier, West Greenland. *The Cryosphere*, *6*(4), 909–922. https://doi.org/10.5194/tc-6-909-2012

Booth, A. D., Emir, E., & Diez, A. (2016). Approximations to seismic AVA responses: Validity and potential in glaciological applications. *Geophysics*, *81*(1), WA1–WA11. https://doi.org/10.1190/geo2015-0187.1

Bougamont, M., Christoffersen, P., Hubbard, A. L., Fitzpatrick, A. A., Doyle, S. H., & Carter, S. P. (2014). Sensitive response of the Greenland Ice Sheet to surface melt drainage over a soft bed. *Nature Communications*, *5*(1), 5052. https://doi.org/10.1038/ncomms6052

Boulton, G. S., Dent, D. D., & Morris, E. M. (1974). Subglacial shearing and crushing, and the role of water pressures in tills from South-East Iceland. *Geografiska Annaler - Series A: Physical Geography*, *56*(3–4), 135–145. https://doi.org/10.2307/520703

Boulton, G. S., & Dent, D. L. (1974). The nature and rates of post-depositional changes in recently deposited till from South-East Iceland. *Geografiska Annaler - Series A: Physical Geography*, *56*(3–4), 121–134. https://doi.org/10.2307/520702

Boulton, G. S., & Paul, M. A. (1976). The influence of genetic processes on some geotechnical properties of glacial tills. *The Quarterly Journal of Engineering Geology*, *9*(3), 159–194. https://doi.org/10.1144/gsl.qjeg.1976.009.03.03

Bradley, S. L., Hindmarsh, R. C., Whitehouse, P. L., Bentley, M. J., & King, M. A. (2015). Low post-glacial rebound rates in the Weddell Sea due to late Holocene ice-sheet readvance. *Earth and Planetary Science Letters*, *413*, 79–89. https://doi.org/10.1016/j.epsl.2014.12.039

Brisbourne, A. M., Martín, C., Smith, A. M., Baird, A. F., Kendall, J. M., & Kingslake, J. (2019). Constraining recent ice flow history at Korff Ice Rise, West Antarctica, using radar and seismic measurements of ice fabric. *Journal of Geophysical Research: Earth Surface*, *124*(1), 175–194. https://doi.org/10.1029/2018JF004776

Brisbourne, A. M., & Smith, A. M. (2018). Multi-azimuth long-offset seismic gathers from Korff Ice Rise, West Antarctica, 2015 (version 1.0) [Dataset]. *Polar Data Centre, Natural Environment Research Council, UK Research & Innovation*. https://doi.org/10.5285/c563569e-0875-404b-acb2-cd5f9e5c4706

Brisbourne, A. M., Smith, A. M., Rivera, A., Zamora, R., Napoleoni, F., Uribe, J. A., & Ortega, M. (2023). Bathymetry and bed conditions of Lago Subglacial CECs, West Antarctica. *Journal of Glaciology*, *69*(278), 1546–1555. https://doi.org/10.1017/jog.2023.38

Brisbourne, A. M., Smith, A. M., Vaughan, D. G., King, E. C., Davies, D., Bingham, R. G., et al. (2017). Bed conditions of Pine Island Glacier, West Antarctica. *Journal of Geophysical Research: Earth Surface*, *122*(1), 419–433. https://doi.org/10.1002/2016JF004033

Carpenter, E. W., Bullard, E. C., & Penney, W. G. (1966). A quantitative evaluation of teleseismic explosion records. *Proceedings of the Royal Society of London - Series A: Mathematical and Physical Sciences*, *290*(1422), 396–407. https://doi.org/10.1098/rspa.1966.0058

Castagna, J. P., & Backus, M. M. (1993). AVO analysis—tutorial and review. *Offset-dependent reflectivity: theory and practice of AVO analysis*, 3–36.

Catania, G. A., Scambos, T. A., Conway, H., & Raymond, C. F. (2006). Sequential stagnation of Kamb ice stream, West Antarctica. *Geophysical Research Letters*, *33*(14). https://doi.org/10.1029/2006GL026430

Červený, V. (1966). On dynamic properties of reflected and head waves in the n-layered earth's crust. *Geophysical Journal of the Royal Astronomical Society*, *11*(1), 139–147. https://doi.org/10.1111/j.1365-246X.1966.tb03496.x

Chandra, R., Riverman, K. L., Pettit, E. C., Schmerr, N. C., Carroll, G., & Bailey, S. H. (2025). Seismic evidence of impact breccia and unlithified sediments under Hiawatha Glacier. *Journal of Geophysical Research: Earth Surface*, *130*(7), e2024JF008247. https://doi.org/10.1029/2024JF008247

Christensen, N. I. (1989). Seismic velocities. In R. S. Carmichael (Ed.), *Practical handbook of physical properties of rocks and minerals*. Boca Raton, Fla.: CRC press.

Clee, T. E., Savage, J. C., & Neave, K. G. (1969). Internal friction in ice near its melting point. *Journal of Geophysical Research*, *74*(4), 973–980. https://doi.org/10.1029/JB074i004p00973

Clyne, E. R., Anandakrishnan, S., Muto, A., Alley, R. B., & Voigt, D. E. (2020). Interpretation of topography and bed properties beneath Thwaites Glacier, West Antarctica using seismic reflection methods. *Earth and Planetary Science Letters*, *550*, 116543. https://doi.org/10.1016/j.epsl.2020.116543

Dawson, E. J., Schroeder, D. M., Chu, W., Mantelli, E., & Seroussi, H. (2022). Ice mass loss sensitivity to the Antarctic ice sheet basal thermal state. *Nature Communications*, *13*(1), 4957. https://doi.org/10.1038/s41467-022-32632-2

Fretwell, P., Pritchard, H. D., Vaughan, D. G., Bamber, J. L., Barrand, N. E., Bell, R., et al. (2013). Bedmap2: Improved ice bed, surface and thickness datasets for Antarctica. *The Cryosphere*, *7*(1), 375–393. https://doi.org/10.5194/tc-7-375-2013

Hank, K., Arthern, R. J., Williams, C. R., Brisbourne, A. M., Smith, A. M., Smith, J. A., et al. (2025). The Antarctic Ice Sheet sliding law inferred from seismic observations. *EGUsphere*, *2025*, 1–22. https://doi.org/10.5194/egusphere-2025-764

Harper, J. T., Humphrey, N. F., Meierbachtol, T. W., Graly, J. A., & Fischer, U. H. (2017). Borehole measurements indicate hard bed conditions, Kangerlussuaq sector, western Greenland Ice Sheet. *Journal of Geophysical Research: Earth Surface*, *122*(9), 1605–1618. https://doi.org/10.1002/2017JF004201

Hastings, W. K. (1970). Monte Carlo sampling methods using Markov chains and their applications. *Biometrika*, *57*(1), 97–109. https://doi.org/10.1093/biomet/57.1.97

He, Y.-X., He, G., Yuan, S., Zhao, J., & Wang, S. (2022). Bayesian frequency-dependent AVO inversion using an improved Markov chain Monte Carlo method for quantitative gas saturation prediction in a thin layer. *IEEE Geoscience and Remote Sensing Letters*, *19*, 1–5. https://doi.org/10.1109/LGRS.2020.3046283

Hillenbrand, C.-D., Bentley, M. J., Stolldorf, T. D., Hein, A. S., Kuhn, G., Graham, A. G., et al. (2014). Reconstruction of changes in the Weddell Sea sector of the Antarctic Ice Sheet since the last Glacial Maximum. *Quaternary Science Reviews*, *100*, 111–136. (Reconstruction of Antarctic Ice Sheet Deglaciation (RAISED)). https://doi.org/10.1016/j.quascirev.2013.07.020

Hofstede, C., Christoffersen, P., Hubbard, B., Doyle, S. H., Young, T. J., Diez, A., et al. (2018). Physical conditions of fast glacier flow: 2. Variable extent of anisotropic ice and soft basal sediment from seismic reflection data acquired on Store Glacier, West Greenland. *Journal of Geophysical Research: Earth Surface*, *123*(2), 349–362. https://doi.org/10.1002/2017JF004297

Hofstede, C., Wilhelms, F., Neckel, N., Fritzsche, D., Beyer, S., Hubbard, A., et al. (2023). The subglacial lake that wasn't there: Improved interpretation from seismic data reveals a sediment bedform at Isunnguata Sermia. *Journal of Geophysical Research: Earth Surface*, *128*(10), e2022JF006850. https://doi.org/10.1029/2022JF006850

Holland, C. W., & Anandakrishnan, S. (2009). Subglacial seismic reflection strategies when source amplitude and medium attenuation are poorly known. *Journal of Glaciology*, *55*(193), 931–937. https://doi.org/10.3189/002214309790152528

Horgan, H. J., van Haastrecht, L., Alley, R. B., Anandakrishnan, S., Beem, L. H., Christianson, K., et al. (2021). Grounding zone subglacial properties from calibrated active-source seismic methods. *The Cryosphere*, *15*(4), 1863–1880. https://doi.org/10.5194/tc-15-1863-2021

Killingbeck, S. F., Livermore, P. W., Booth, A. D., & West, L. J. (2018). Multimodal layered transdimensional inversion of seismic dispersion curves with depth constraints. *Geochemistry, Geophysics, Geosystems*, *19*(12), 4957–4971. https://doi.org/10.1029/2018GC008000

Killingbeck, S. F., Rutishauser, A., Unsworth, M. J., Dubnick, A., Criscitiello, A. S., Killingbeck, J., et al. (2024). Misidentified subglacial lake beneath the Devon Ice Cap, Canadian Arctic: A new interpretation from seismic and electromagnetic data. *The Cryosphere*, *18*(8), 3699–3722. https://doi.org/10.5194/tc-18-3699-2024

Kingslake, J., Martín, C., Arthern, R. J., Corr, H. F. J., & King, E. C. (2016). Ice-flow reorganization in West Antarctica 2.5 kyr ago dated using radar-derived englacial flow velocities. *Geophysical Research Letters*, *43*(17), 9103–9112. https://doi.org/10.1002/2016GL070278

Kingslake, J., Scherer, R. P., Albrecht, T., Coenen, J., Powell, R. D., Reese, R., et al. (2018). 01). Extensive retreat and re-advance of the West Antarctic ice sheet during the Holocene. *Nature*, *558*(7710), 430–434. https://doi.org/10.1038/s41586-018-0208-x

Kirchner, J. F., & Bentley, C. R. (1979). Seismic short-refraction studies on the Ross Ice Shelf, Antarctica. *Journal of Glaciology*, *24*(90), 313–319. https://doi.org/10.3189/S0022143000014830

Knott, C. G. (1899). Reflexion and refraction of elastic waves with seismological applications. *Philosophical magazine*.

Kohnen, H. (1972). Über die Beziehung zwischen seismischen Geschwindigkeiten und der Dichte in Firn und Eis. *Zeitschrift für Geophysik*, *38*(5), 925–935.

Komatitsch, D., Tromp, J., Gharti, H. N., Peter, D., Cano, E. V., Bachmann, E., et al. (2023). Specfem/specfem2d: Specfem2d v8.1.0 (v8.1.0) [software]. *Zenodo*. https://doi.org/10.5281/zenodo.10415228

Kulessa, B., Hubbard, A. L., Booth, A. D., Bougamont, M., Dow, C. F., Doyle, S. H., et al. (2017). Seismic evidence for complex sedimentary control of Greenland Ice Sheet flow. *Science Advances*, *3*(8), e1603071. https://doi.org/10.1126/sciadv.1603071

Kurt, H. (2007). Joint inversion of AVA data for elastic parameters by bootstrapping. *Computers & Geosciences*, *33*(3), 367–382. https://doi.org/10.1016/j.cageo.2006.08.012

Kyrke-Smith, T. M., Gudmundsson, G. H., & Farrell, P. E. (2017). Can seismic observations of bed conditions on ice streams help constrain parameters in ice flow models? *Journal of Geophysical Research: Earth Surface*, *122*(11), 2269–2282. https://doi.org/10.1002/2017JF004373

Labedz, C. R., Bartholomaus, T. C., Amundson, J. M., Gimbert, F., Karplus, M. S., Tsai, V. C., & Veitch, S. A. (2022). Seismic mapping of subglacial hydrology reveals previously undetected pressurization event. *Journal of Geophysical Research: Earth Surface*, *127*(3), e2021JF006406. https://doi.org/10.1029/2021JF006406

Lu, J., Yang, Z., Wang, Y., & Shi, Y. (2015). Joint PP and PS AVA seismic inversion using exact Zoeppritz equations. *Geophysics*, *80*(5), R239–R250. https://doi.org/10.1190/geo2014-0490.1

Margrave, G., & Lamoureux, M. (2019). *Numerical methods of exploration seismology: With algorithms in MATLAB®*. Cambridge University Press.

Metropolis, N., Rosenbluth, A. W., Rosenbluth, M. N., Teller, A. H., & Teller, E. (1953). Equation of state calculations by fast computing machines. *The Journal of Chemical Physics*, *21*(6), 1087–1092. https://doi.org/10.1063/1.1699114

Mulvaney, R., Rix, J., Polfrey, S., Grieman, M., Martìn, C., Nehrbass-Ahles, C., et al. (2021). Ice drilling on skytrain ice rise and Sherman Island, Antarctica. *Annals of Glaciology*, *62*(85–86), 311–323. https://doi.org/10.1017/aog.2021.7

Muto, A., Anandakrishnan, S., Alley, R. B., Horgan, H. J., Parizek, B. R., Koellner, S., et al. (2019). Relating bed character and subglacial morphology using seismic data from Thwaites Glacier, West Antarctica. *Earth and Planetary Science Letters*, *507*, 199–206. https://doi.org/10.1016/j.epsl.2018.12.008

Neuhaus, S. U., Tulaczyk, S. M., Stansell, N. D., Coenen, J. J., Scherer, R. P., Mikucki, J. A., & Powell, R. D. (2021). Did holocene climate changes drive West Antarctic grounding line retreat and readvance? *The Cryosphere*, *15*(10), 4655–4673. https://doi.org/10.5194/tc-15-4655-2021

Nolan, M., & Echelmeyer, K. (1999). Seismic detection of transient changes beneath Black rapids Glacier, Alaska, U.S.A.: II. Basal morphology and processes. *Journal of Glaciology*, *45*(149), 132–146. https://doi.org/10.3189/S0022143000003117

Pan, X.-O., Zhang, G.-Z., Zhang, J.-J., & Yin, X.-Y. (2017). 01). Zoeppritz-based AVO inversion using an improved Markov chain Monte Carlo method. *Petroleum Science*, *14*(1), 75–83. https://doi.org/10.1007/s12182-016-0131-4

Parizek, B. R., Christianson, K., Anandakrishnan, S., Alley, R. B., Walker, R. T., Edwards, R. A., et al. (2013). Dynamic (in)stability of Thwaites Glacier, West Antarctica. *Journal of Geophysical Research: Earth Surface*, *118*(2), 638–655. https://doi.org/10.1002/jgrf.20044

Peters, L. E., Anandakrishnan, S., Alley, R. B., & Smith, A. M. (2007). Extensive storage of basal meltwater in the onset region of a major West Antarctic ice stream. *Geology*, *35*(3), 251. https://doi.org/10.1130/G23222A.1

Peters, L. E., Anandakrishnan, S., Alley, R. B., Winberry, J. P., Voigt, D. E., Smith, A. M., & Morse, D. L. (2006). Subglacial sediments as a control on the onset and location of two Siple Coast ice streams, West Antarctica. *Journal of Geophysical Research*, *111*(B1). https://doi.org/10.1029/2005JB003766

Peters, L. E., Anandakrishnan, S., Holland, C. W., Horgan, H. J., Blankenship, D. D., & Voigt, D. E. (2008). Seismic detection of a subglacial lake near the South Pole, Antarctica. *Geophysical Research Letters*, *35*(23), L23501. https://doi.org/10.1029/2008GL035704

Picotti, S., Carcione, J. M., & Pavan, M. (2024). Seismic attenuation in Antarctic firn. *The Cryosphere*, *18*(1), 169–186. https://doi.org/10.5194/tc-18-169-2024

Ramos, A. C. B., & Castagna, J. P. (2001). Useful approximations for converted-wave AVO. *Geophysics*, *66*(6), 1721–1734. https://doi.org/10.1190/1.1487114

Smith, A. M. (1997a). Basal conditions on Rutford Ice Stream, West Antarctica, from seismic observations. *Journal of Geophysical Research*, *102*(B1), 543–552. https://doi.org/10.1029/96JB02933

Smith, A. M. (1997b). Variations in basal conditions on Rutford Ice Stream, West Antarctica. *Journal of Glaciology*, *43*(144), 245–255. https://doi.org/10.3189/S0022143000003191

Tromp, J., Komatitsch, D., & Liu, Q. (2008). Spectral-element and adjoint methods in seismology. *Communications in Computational Physics*, *3*(1), 1–32.

Ursenbach, C. (2005). Can multicomponent or joint AVO inversion improve impedance estimates? In *Seg technical program expanded abstracts* (Vol. 2003, pp. 161–164). https://doi.org/10.1190/1.1817612

Veitch, S. A., Karplus, M., Kaip, G., Gonzalez, L. F., Amundson, J. M., & Bartholomaus, T. C. (2021). Ice thickness estimates of Lemon Creek Glacier, Alaska, from active-source seismic imaging. *Journal of Glaciology*, *67*(265), 824–832. https://doi.org/10.1017/jog.2021.32

Voigt, D. E., Peters, L. E., & Anandakrishnan, S. (2013). Georods': The development of a four-element geophone for improved seismic imaging of glaciers and ice sheets. *Annals of Glaciology*, *54*(64), 142–148. https://doi.org/10.3189/2013AoG64A432

Wearing, M. G., & Kingslake, J. (2019). Holocene formation of Henry Ice Rise, West Antarctica, inferred from ice-penetrating radar. *Journal of Geophysical Research: Earth Surface*, *124*(8), 2224–2240. https://doi.org/10.1029/2018JF004988

Zechmann, J. M., Booth, A. D., Truffer, M., Gusmeroli, A., Amundson, J. M., & Larsen, C. F. (2018). Active seismic studies in valley glacier settings: Strategies and limitations. *Journal of Glaciology*, *64*(247), 796–810. https://doi.org/10.1017/jog.2018.69

Zoeppritz, K. (1919). VII b. Über Reflexion und Durchgang seismischer Wellen durch Unstetigkeitsflächen. Nachrichten von der Gesellschaft der Wissenschaften zu Göttingen. *Mathematisch-Physikalische Klasse*, *1919*, 66–84.